Chapter 9

OPTIMAL CONTROL OF ATOMIC, MOLECULAR AND ELECTRON DYNAMICS WITH TAILORED FEMTOSECOND LASER PULSES

Tobias Brixner, Thomas Pfeifer and Gustav Gerber
Physics Department, University of Würzburg
Am Hubland, 97074 Würzburg, Germany

Matthias Wollenhaupt and Thomas Baumert
Institute of Physics, University of Kassel
Heinrich-Plett-Str. 40, 34132 Kassel, Germany

Abstract With the invention of the laser, the dream was realized to actively exert control over quantum systems. Active control over the dynamics of quantum mechanical systems is a fascinating perspective in modern physics. Cleavage and creation of predetermined chemical bonds, selective population transfer in atoms and molecules, and steering the dynamics of bound and free electrons have been important milestones along this way. A promising tool for this purpose is available with femtosecond laser technologies. In this chapter we review some of our work on adaptive femtosecond quantum control where a learning algorithm and direct experimental feedback signals are employed to optimize user-defined objectives. Femtosecond laser pulses are modified in frequency-domain pulse shapers, which apart from phase- and intensity-modulation can also modify the polarization state as a function of time. We will highlight the major advances in the field of optimal control by presenting our own illustrative experimental examples such as gas-phase and liquid-phase femtochemistry, control in weak and strong laser fields, and control of electron dynamics.

Key words: Optimal control, coherent control, femtosecond laser-pulse shaping, femtochemistry, gas-phase/liquid phase photochemistry, electron dynamics, high-order harmonic generation, intense ultrashort laser-matter interaction.

1. INTRODUCTION

Since the early days of quantum mechanics there has been a desire to "understand" in detail the general behavior of quantum systems. This quest has been accompanied by the implicit dream not only to be able to observe in a passive way, but in fact also to actively control quantum mechanical processes. The key question in quantum control is: Can one find external control parameters which guide the temporal evolution of quantum-mechanical systems in a desired way, even if this evolution is very complex? The theoretical and experimental development of suitable control schemes is a fascinating prospect of modern physics.

Immediate applications are found in many different branches of scientific and engineering research. A selected but by no means comprehensive list of examples includes applications in photochemistry (microscopic control of chemical reactions), quantum optics (optimized generation of high-harmonic soft X-rays), atomic and molecular physics (wavepacket shaping and selective photo-excitation), biophysics (optimization of nonlinear imaging techniques), solid-state physics (coherent current control), tele-communications (optical signal encoding), or applications in related quantum technologies (such as quantum computing or quantum cryptography). But, in addition to these direct benefits, the successful implementation of quantum control concepts is also likely to provide new insights into the intricacies of the underlying quantum mechanical dynamics.

The required temporal structure of the control fields is tied to the timescale of quantum mechanical motion. Focusing on chemical reaction dynamics, this timescale is determined by the atomic motions within their molecular frameworks and has been made accessible to experiment by the development during the last 20 years of femtosecond laser technology. Ultrashort light pulses can now be used to follow in real-time the primary events of many chemical – and also physical or biological – processes. The emerging field in the area of chemistry has been accordingly termed "femtochemistry", and Ahmed Zewail has received the Nobel Prize in Chemistry in 1999 "for his studies of the transition states of chemical reactions using femtosecond spectroscopy" [1].

The combination of quantum control with femtosecond laser spectroscopy – femtosecond quantum control – is a new research field which goes beyond "simple" observation, seeking to *control* chemical reactions by suitably "shaped" femtosecond light fields. In this way, it is possible to influence product distributions in such a way that the generation of desired products is enhanced while the formation of unwanted by-products is simultaneously reduced. In contrast to the methods used in "conventional" chemistry, this is done on a "microscopic" level – directly in the investigated

molecule – by forcing the dynamical evolution of quantum wavefunctions into the desired direction. A number of recent review articles and books have treated the subject of quantum control from different perspectives [2-10].

In this chapter, we illustrate fundamental concepts and mechanisms of quantum control on prototypal small systems and then discuss the principles and applications of adaptive control on large systems with many degrees of freedom. And although we take the experimental examples from our own research, we point out that other groups have also contributed significantly to the rapidly evolving field of coherent control. Applications of the closed-loop learning scheme to molecular systems were first demonstrated in a population-transfer experiment by Bardeen et al. [11] and our group was then the first to realize automated quantum control of photodissociation reactions in complex molecules [12]. Other early examples of the adaptive scheme include the excitation of different vibrational modes in a molecular liquid [13] and the control of vibrational dynamics in a four-wave mixing experiment [14].

But optimal quantum control is not limited to molecular systems. Femtosecond laser pulse shapers and learning loops have been used for automated pulse compression [15-17] and optimized generation of arbitrary laser pulse shapes [18, 19], control of two-photon transitions in atoms [20, 21], shaping of Rydberg wavepackets [22], optimization of high-harmonic generation [23, 24], and control of ultrafast semiconductor nonlinearities [25]. Shaped electric fields have also been suggested to be of use in the context of laser cooling [26]. Furthermore, recent developments include the transfer of adaptive control methods to achieve selective photoexcitation in the liquid phase [27, 28], control over energy transfer even in a biological system [29], and the optimization of Raman-type nonlinear spectroscopy and microscopy [30].

This chapter is structured as follows: In Sect. 2 we introduce and demonstrate simple one-parameter control schemes. Simple atomic and molecular systems are the subject of the investigations presented, since they can be almost fully understood by theoretical approaches. Section 3 deals with more complex molecules in the gas phase, which are harder to understand through modeling. Therefore, many-parameter control schemes have to be introduced in order to steer those systems into the desired target states. Increasing the density of the particles in the experiment leads us into the liquid phase in Sect. 4, where control is partially impaired through loss of coherence due to solute-solvent interactions. We show that this problem can be addressed by using adaptive laser-pulse shaping. Finally, Sect. 5 shows that we are not limited to controlling atomic and molecular excitation. We show that transfer of coherence to electrons and electronic motion can be controlled, paving the way for a new era of optimal control.

2. ONE-PARAMETER CONTROL ON PROTOTYPES: ATOMS AND DIMERS IN THE GAS PHASE

Currently, much attention is focused on the utilization of adaptive feedback-controlled femtosecond pulse shaping making available a most versatile instrument for multi-parameter control schemes [12, 23, 28, 29, 31-34]. These techniques (see also Sects. 3-5) have proven to be universal in the sense that they enable the optimization of virtually any conceivable quantity and are capable of delivering the optimal electric field without knowledge of the underlying potential energy surface. However, the individual control mechanisms may be inferred, if only for very simple systems. In order to obtain a better physical insight into such a multi-parameter control scenario it is essential to investigate one-parameter control schemes in detail on pertinent model systems.

The choice of a suitable model system is governed by several requirements: in order to support the validity of the physical pictures of the control process full quantum-mechanical simulations of the experiment should be feasible. Therefore, "computable" systems such as diatomic molecules (or atoms) are most workable. Moreover, a detailed knowledge of all electronic states involved is a prerequisite. Insight into the dynamics of the control can be accomplished if the experiment allows structural and electronic changes in the configuration to be monitored with high spatial and temporal resolution. Measurements of kinetic photo-electrons using time-of-flight (TOF) spectrometry combined with a femtosecond multiphoton ionization pump-probe technique on Na_2 in a molecular beam allows molecular motion to be mapped with sub-Ångström spatial and femtosecond temporal resolution [35]. Therefore, such an approach is ideally suited for detailed studies of how quantum control can be achieved. In general, ionization techniques in combination with femtosecond pump-probe techniques have the advantage that the limitation of the probe transition to a localized Franck-Condon window is overcome and that due to the mass sensitivity a detailed product analysis can be performed. In addition, kinetic energy time-of-flight (KETOF) spectroscopy on the product species [36, 37] as well as zero electron kinetic energy (ZEKE) techniques [38] have been employed in that context.

Published examples from our own work for such one-parameter control schemes elucidating the mechanism of quantum control are presented. The general topic has been detailed in recent textbooks [4, 39].

2.1 Control in the Perturbative Limit

In the range where the Rabi frequency Ω_R is smaller than $2\pi/T$, where T is the interaction time, the light-matter interaction is usually described with help of perturbation theory. In a one-photon process this regime does not allow control over a final-state population [40] although during the interaction an interesting population dynamics is observed [41]. Here, we discuss multi-photon ionization of the Na_2 molecule with respect to control. We start with a description of the excitation scheme before we discuss the so-called Tannor-Kosloff-Rice scheme and the influence of simple shaped laser pulses.

2.1.1 Excitation scheme

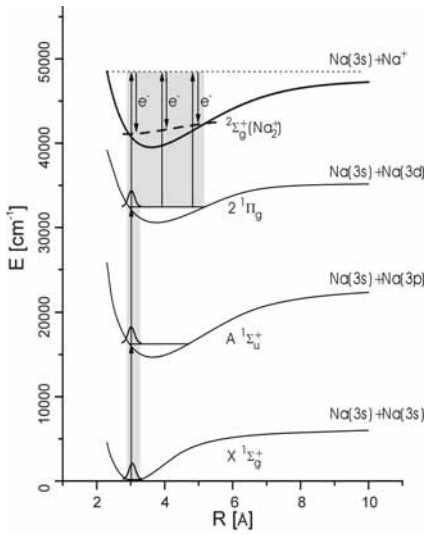

Figure 9-1. Excitation scheme for the Na_2 molecule. The pump laser in the range of 620 nm creates wave packets in the A $^1\Sigma_u^+$ and the 2 $^1\Pi_g$ at the inner turning points. The time-delayed probe laser ionizes the sodium dimer. As indicated, the kinetic energy of the photo-electrons depends on the internuclear coordinate because of the monotonic increasing difference potential (dashed line, see text).

The excitation scheme of the experiment is depicted in Fig. 9-1. At 620 nm three photons are needed to ionize the Na_2 molecule from its neutral ground state X $^1\Sigma_g^+$ into its ionic ground state $^2\Sigma_g^+$. The dynamical aspect of this multi-photon excitation has been investigated in this wavelength regime in detail with ion detection [42]. Due to the spectral width of the laser pulse and due to the Franck-Condon principle one-photon excitation prepares a wave- packet at the inner turning point of the A $^1\Sigma_u^+$ state potential by

coherent superposition of vibrational levels. The round-trip time of this wave-packet is about 310 fs (≈ 110 cm^{-1}). Two-photon excitation leads to preparation of a wave packet at the inner turning point of the 2 $^1\Pi_g$ state potential with a roundtrip time of about 370 fs (≈ 90 cm^{-1}). In Ref. 42, it was found that the A $^1\Sigma_u^+$ state wave-packet motion is reflected in the total Na_2^+ ion yield due to a resonance-enhanced "direct" photo-ionization process via the 2 $^1\Pi_g$ state into the Na_2^+ ($^2\Sigma_g^+$) state at the inner turning point of the molecular potential curves involved. In those experiments the 2 $^1\Pi_g$ state wave-packet motion could only be detected in the Na_2^+ and Na^+ fragment signal due to the excitation of a doubly excited neutral state of the Na_2 molecule near the outer turning point of the 2 $^1\Pi_g$ state potential (not shown in Fig. 9-1) and its subsequent decay channels as auto-ionization (indirect photo-ionization) and auto-ionization-induced fragmentation [42]. Note that "direct" photo-ionization out of the 2 $^1\Pi_g$ state into the Na_2^+ $^2\Sigma_g^+$ state cannot provide the dynamical information on the wave-packet prepared in this state when detected by the total Na_2^+ ion yield, since a large part of the internuclear distances is sampled in a pump-probe experiment [43, 44]. However, by the detection of kinetic energy resolved photo-electrons this dynamical information is obtained, because electrons of different kinetic energies are formed at different internuclear distances. In such a direct photo-ionization process the released kinetic energy of the photo-electrons can be determined by a classical difference potential analysis [45]. Let E_1 and E_2 denote the total energy of the nuclei in molecular potentials $V_1(R)$ and $V_2(R)$ before and after the absorption of a photon with energy hν. Due to the Franck-Condon principle the nuclei will not noticeably change either their relative position or their velocities during an electronic transition. This means the transition occurs at a fixed internuclear distance and will conserve the kinetic energy $E_{kin}(R)$. For a transition between neutral states the energy net result can be written:

$$V_1(R) + E_{kin}(R) + h\nu = V_2(R) + E_{kin}(R) \Leftrightarrow V_2(R) - V_1(R) = h\nu.$$

The classical transition is graphically simply given by the intersection of a horizontal line with height hν with the difference potential $V_2(R) - V_1(R)$. Considering transitions between a neutral and an ionic state we have to modify this analysis slightly, as the ejected electron carries away the excess kinetic energy $E_{electron}$ and we obtain $V_2(R) - V_1(R) = h\nu - E_{electron} \leq h\nu$. It is convenient to shift the difference potential with respect to E_1, so that we can analyse the excitation within the potential energy diagram. The dashed line in Fig. 9-1 displays the difference potential $^2\Sigma_g^+$ (Na_2^+) – 2 $^1\Pi_g$ + 2 hν relevant for this experiment. Within this concept, the expected photo-electron energy in this photo-ionization process out of the 2 $^1\Pi_g$ state

is decreasing with increasing internuclear distance. At the inner turning point of the potential curve photo-electrons of about 0.94 eV are formed where at the outer turning point photo-electrons of about 0.78 eV are released. By recording transient photo-electron spectra the molecular wave-packet motion on neutral electronic states along all energetically allowed internuclear distances is probed simultaneously. Note that the autoionization processes of the doubly excited state lead to photo-electrons with less than 0.5 eV kinetic energy [36], which can be separated from the electrons released in the "direct" photo-ionization process.

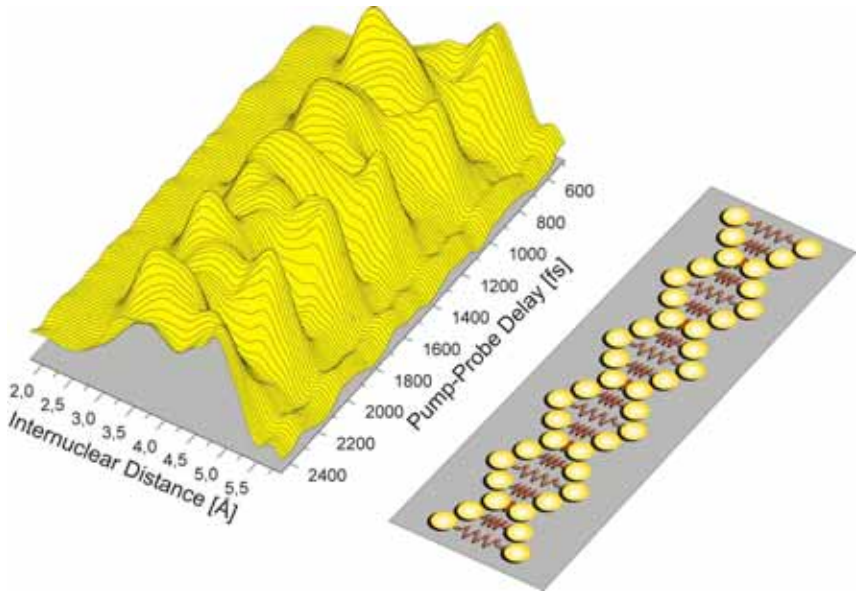

Figure 9-2. After calibration of the spectrometer with the help of atomic resonances, the measured TOF axis is converted into an energy axis. Taking the difference potential into account the mapped wave-packet dynamics as a function of the internuclear distance is obtained with sub-Å spatial resolution. The corresponding harmonic oscillation of a classical diatomic is shown for comparison.

In Fig. 9-2 the measured photo-electron distribution is shown as a function of the pump-probe delay for the same intensity ($I_0 \approx 10^{11}$ W/cm^2, 70 fs, 620 nm) of pump and probe laser. By the variation of the pump-probe delay the dynamics of the molecule in the two neutral states $2\ ^1\Pi_g$ and $A\ ^1\Sigma_u^+$ (via the $2\ ^1\Pi_g$) is monitored. In particular, the propagation of the $2\ ^1\Pi_g$ wave-packet between the turning points is resolved. In order to obtain the mapped wave-packet dynamics as a function of the internuclear distance R we have transformed the TOF axis to the corresponding kinetic energy axis and used the difference potential $^2\Sigma_g^+$ (Na_2^+) – $2\ ^1\Pi_g$. Taking the slope of the

difference potential, the energy resolution of our spectrometer and the spectral width of our fs laser pulses into account, we obtain a spatial resolution of about 0.5 Å.

2.1.2 Control via the Tannor-Kosloff-Rice scheme

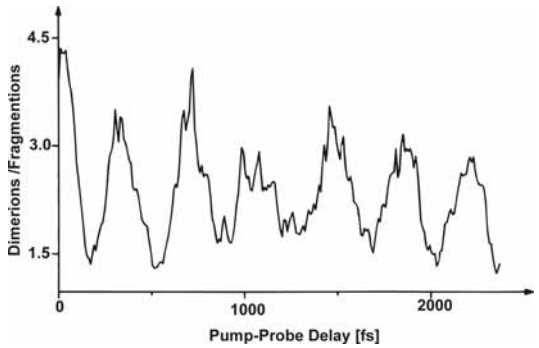

Figure 9-3. Ratio of Na^+ and Na_2^+ ion signals as a function of pump-probe delay. At the outer turning point of the 2 $^1\Pi_g$ state the wave-packet is excited to a doubly excited neutral state that decays *inter alia* via fragmentation. Data are taken from Ref. 42.

In the time domain the so-called Tannor-Kosloff-Rice scheme [46] is a very illustrative way of how to obtain control over different products via photo-excitation of a molecule. They have proposed that controlling the time duration of a wave-packet on an excited electronic potential energy surface can be used to achieve different products. In practice, this means that a pump laser will prepare a vibrational wave-packet on an electronic excited potential and with the help of a time-delayed probe laser the product state will be populated either by dumping the wave-packet down again or by further excitation. In the case studied here we obtain a higher kinetic energy of photo-electrons at the inner turning point and a lower kinetic energy of the photo-electrons at the outer turning point from the ionization of a vibrational wave-packet propagating in the 2 $^1\Pi_g$ state (see Fig. 9-1). If we consider electrons with different energy as different photo-products it is evident from Fig. 9-2 that by controlling the duration of the wave-packet in the 2 $^1\Pi_g$ state we have access to different product states. Note that at the outer turning point we have access to a doubly excited neutral state that decays *inter alia* via fragmentation . By this means we were able to control the photo-product ratio Na^+/Na_2^+ in a pump-probe experiment (see Fig. 9-3) [47, 48]. Further early experimental examples employing this scheme can be found, for example, in the NaI molecule [49] and in the XeI [50] system. Indications that control of wave-packet propagation is an important parameter in adaptive feedback experiments have been reported [34, 51].

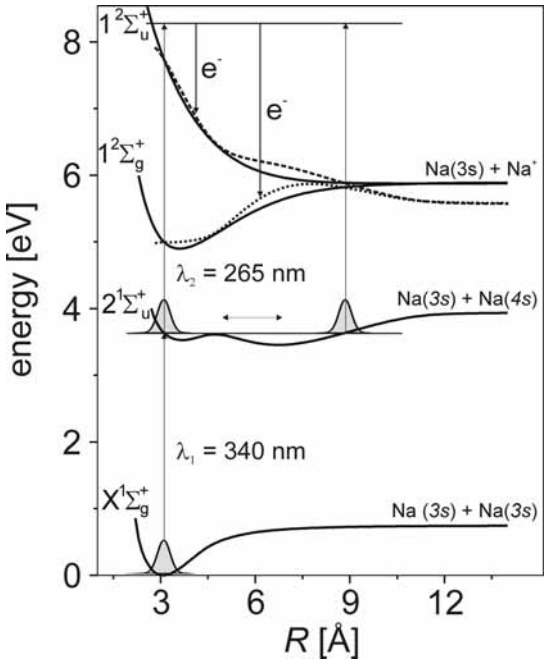

Figure 9-4. Potential energy curves for $\lambda_1 = 340$ nm excitation of the $2\ ^1\Sigma_u^+$ double-minimum state (pump) in Na_2 and subsequent $\lambda_2 = 265$ nm ionization to the bound $1\ ^2\Sigma_g^+$ and repulsive $1\ ^2\Sigma_u^+$ ionic states (probe). The corresponding difference potentials for the bound (dotted) and the repulsive (dashed) ionic states are displayed. Energy resolved photo-electron spectra from both ionic states are measured.

Another aspect in quantum control is introduced by non-adiabatic coupling of the potential curves involved in the time evolution of a quantum system [52]. The coupling of the covalent and ionic potentials in NaI is a prominent example (Ref. 53, and references therein). Electronic changes along the internuclear coordinate (R) are also predicted for the $2\ ^1\Sigma_u^+$ double-minimum potential well in the Na_2 molecule (Fig. 9-4). According to theory [54] the change of electronic structure near the avoided crossing at 4.7 Å leads to photo-ionization probabilities rapidly changing with geometry. Our approach to measuring the R-dependent photo-ionization probabilities is based on the comparison of simulated photo-electron spectra assuming an R-independent ionization probability and measured data. We performed a two-color ($\lambda_1 = 340$ nm pump and $\lambda_2 = 265$ nm probe) pump-probe experiment (see Fig. 9-4). At an excitation wavelength of 340 nm, the generated wave-packet oscillates between 3 and 9 Å and thus samples the inner Rydberg region and the outer well which has ionic character at large internuclear distances [55]. The ionization probe wavelength of 265 nm was chosen (i) to map the complete energetically allowed range of internuclear distances, and

(ii) to simultaneously project the wave-packet motion onto the 1 $^2\Sigma_g^+$ bound and the 1 $^2\Sigma_u^+$ repulsive ionic state. Since the photo-electron spectra directly reveal the ionization pathway, competing ionization processes can be identified or ruled out [56]. More sophisticated information about the time evolution of the molecular electronic structure could be obtained with the use of angle-resolved photo-electron spectroscopy, in principle, as was studied theoretically [54, 57] and also demonstrated experimentally [58, 59].

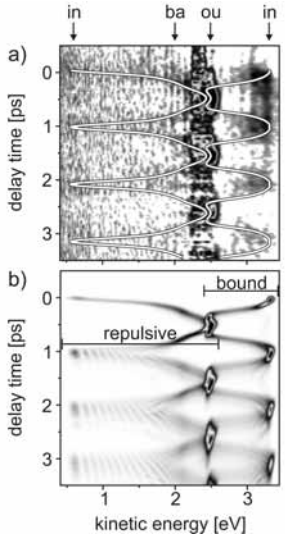

Figure 9-5. (a) Measured and (b) calculated time evolution of photo-electron spectra for λ_1 = 340 nm excitation and λ_2 = 265 nm ionization. The kinetic energy for inner (in) and outer (ou) turning point and the barrier (ba) is indicated with arrows. Photo-electrons from the repulsive and bound ionic state are observed at 0.4 - 2.6 eV and 2.4 - 3.5 eV, respectively (indicated by horizontal bars). Electrons from both ionic states formed at the outer turning point overlap at 2.5 eV. To guide the eye the measured signal is superimposed by the electron energies obtained by classical trajectory calculation and difference potential analysis (white line in (a)).

Figure 9-5a shows a grey-scale representation of the measured photo-electron spectra obtained within the first 3.5 ps time delay between pump and probe pulses. To enhance the visibility of the measured signal the kinetic energy for "classical electrons" is superimposed as a white line in Fig. 9-5a. For this purpose, classical trajectory calculations were performed to model the wave-packet motion and the corresponding photo-electron energies were obtained from difference potential analysis. For comparison the quantum-mechanically calculated photo-electron distributions from both the bound 1 $^2\Sigma_g^+$ and repulsive 1 $^2\Sigma_u^+$ ionic states are depicted in Fig. 9-5b.

The variation of μ(R) is observed such that (i) ionization to the bound ionic state is favored at all internuclear distances, and (ii) for the bound ionic state the ionization probability at the outer turning point is 4.0 ± 0.4 times larger than at the inner turning point. Our results demonstrate the utilization of wave-packets as a local probe for an R-dependent ionization probability and in particular the usefulness of energy-resolved photo-electron detection to unambiguously identify the ionization pathway. A detailed discussion of the results is given in Ref. 56.

2.1.3 Control via simple shaped pulses

In the following we report on a strong chirp dependence of the three-photon ionization probability of Na_2 using simple phase-shaped femtosecond laser pulses in the excitation scheme of Fig. 9-1. We will see that both pulse duration and phase modulation of an ultrashort pulse are active control parameters. We show that for a certain chirp a higher ionization yield in the multi-photon process is observed when simultaneously the population in the intermediate states is minimal. As this experiment is performed in the perturbative regime the physical mechanisms of rapid adiabatic passage [60], by which 100 % population transfer can be achieved with chirped laser pulses, is not operative. For a detailed discussion of our experiment see Ref. 61.

Figure 9-6 shows photo-electron spectra obtained from ionizing Na_2 with up-chirped (increasing laser frequency with time) and down-chirped (decreasing laser frequency with time) laser pulses at 620 nm. The chirped pulses were produced by increasing or decreasing the optical pathway in a prism sequence (SF10) that is used to compress the pulses coming out of an optical parametric generator (OPG) down to their transform limit of 40 fs. The upper and lower spectra in Fig. 9-6a were obtained with linearly chirped pulses (3500 ± 500 fs^2), which corresponds to a pulse duration of approximately 240 fs.

The ionization yield is seen to double when the frequency order is switched from blue first to red first within the exciting laser pulse. Note that the up- and down-chirped pulses are identical in all their pulse parameters, except for being reversed in time. This indicates that the change in the electron spectra is indeed due to the phase modulation and not to other effects such as different pulse durations or different intensity distributions. In order to better understand the experimental results, we performed quantum mechanical calculations following the method employed in Refs. 62 and 63. We included the electric field of a linearly chirped Gaussian laser pulse in analytical form (see, e.g., Ref. 64). In accordance with the experimental conditions (the laser beam was attenuated appropriately) calculations were

performed in the weak-field limit taking into account the X $^1\Sigma_g^+$, A $^1\Sigma_u^+$ and 2 $^1\Pi_g$ neutral electronic states and coupling the 2 $^1\Pi_g$ state to the continuum of the ionic ground state $^2\Sigma_g^+$ (Na_2^+). R-independent dipole matrix elements were assumed for all transitions. The calculated electron spectra depicted in Fig. 9-6b qualitatively reproduce the measured results. In addition, the population in the 2 $^1\Pi_g$ state as a function of time was calculated for both chirp directions, which is shown in Fig. 9-6c.

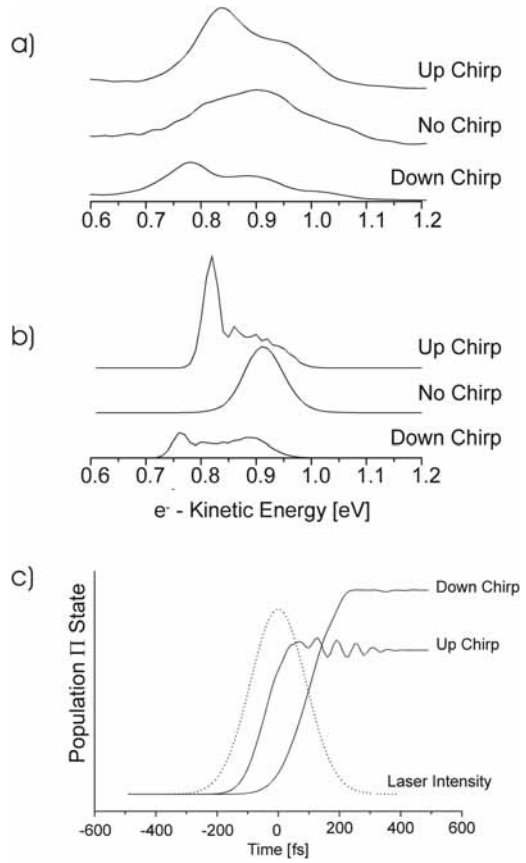

Figure 9-6. a) Electron spectra measured with single up-chirped (+3500 fs^2), down-chirped (– 3500 fs^2) and unchirped laser pulses. The transform-limited pulses of 40 fs duration are centered at a wavelength of 618 nm. The chirped pulses are of 240 fs duration. b) Calculated spectra using the same parameters as above. c) Calculated temporal development of the population in the 2 $^1\Pi_g$ state during interaction with up- and down-chirped laser pulses (± 3500 fs^2). The chirped pulse profile is shown as a dotted line.

Since the Franck-Condon maximum for both the A $^1\Sigma_u^+ \leftarrow$ X $^1\Sigma_g^+$ state transition as well as for the 2 $^1\Pi_g \leftarrow$ A $^1\Sigma_u^+$ state transition is shifted towards

the red of the central laser wavelength, the up-chirped laser pulse transfers population to the excited states earlier, while a down-chirped laser pulse can efficiently excite the intermediate states only with its trailing edge. For the subsequent ionization process this temporal behavior is essential. In order to achieve a high ionization yield the population in the $2\ ^1\Pi_g$ state must be high at the maximum laser intensity, which is achieved with up-chirped but not with down-chirped laser pulses.

However, Fig. 9-6c also yields a very surprising result. The total population transferred to the $2\ ^1\Pi_g$ state after the end of the pulse is much larger for a down-chirped laser although the ionization yield with this pulse is smaller. This is not due to population transfer to the ionic ground state since in the weak-field limit ionization does not (significantly) decrease the neutral state population. Rather, a mechanism very similar to that in the experiments described in Ref. 65 is responsible for this effect. To understand this a semiclassical argument based on the difference potential analysis is very illuminating. When a chirped laser pulse is used, the photon energy $h\nu$ is changing in time. For a down-chirped pulse the decreasing laser frequency follows the decrease in the difference potential $2\ ^1\Pi_g$ - $A\ ^1\Sigma_u^+$ (not shown in Fig. 9-1) as the excited-state wave-packet propagates to larger internuclear distances. Excitation is "synchronized" to the wave-packet motion over a wider range of the nuclear coordinate for a down-chirped laser pulse and the corresponding final population in the $2\ ^1\Pi_g$ state is higher. With the opposite chirp direction (up chirp), on the other hand, one observes a higher ionization yield while the intermediate state population is kept low. This kind of optimization is desired in coherent control schemes, because this is a prototype of simultaneous maximization versus minimization of photo-products. Besides the strong chirp dependence of the ionization yield observable in the electron spectra of Fig. 9-6a and 9-6b, a very different electron signal is observed for unchirped 40 fs laser pulses compared to the chirped laser pulses of 240 fs duration (3500 fs^2). The short laser pulse predominantly yields electrons with kinetic energy of about 0.9 eV, while the electron spectra obtained with the longer (chirped) pulses are dominated by electrons around 0.8 eV. This behavior can again be understood by a difference potential analysis, this time for the transition from the $2\ ^1\Pi_g$ state to the ionic ground state (see Fig. 9-1).

Since the difference potential is increasing with internuclear distance, the electrons released have less kinetic energy when formed at the outer turning point of a wave-packet propagating in the $2\ ^1\Pi_g$ potential than those formed at the inner turning point (see Fig. 9-1). The duration of the transform-limited 40 fs pulse is much shorter than the oscillation period (approx. 370 fs) of the wave-packet for the excited $2\ ^1\Pi_g$ state, and the wave-packet has no time to move to large internuclear distances during the laser

interaction. The up- and down-chirped laser pulses, however, are of much longer duration, which allows the wave-packets to sweep the whole range of allowed internuclear distances while ionization takes place. The resulting electron spectra therefore extend to lower kinetic energies, which correspond to the outer turning point where the wave-packets spend more time.

Taking the pulse duration as an active control parameter is also operative in larger molecules as demonstrated in the fragmentation of $Fe(CO)_5$ [66].

2.2 Control in Strong Laser Fields

We now turn to the topic of strong-field interaction characterized by the Rabi frequency Ω_R being larger than $2\pi/T$, where T is the interaction time.

2.2.1 Coherent coupling of molecular electronic states

In general, the wavelength range needed for the excitation of an intermediate state will differ from the wavelength range to reach the product state at a certain bond configuration. If the two wavelength regimes are not contained within the spectral width of the laser pulse a weak-field approach may not be efficient. A solution can be found by utilizing intensity-dependent effects as was demonstrated for Na_2 [67, 68]. Such effects are also expected to be operative in the adaptive feedback approach for larger molecules [12, 32, 69]. In our prototype measurements, according to the excitation scheme in Fig. 9-1, the pump laser intensity is kept fixed at $I_0 \approx 10^{11}$ W/cm^2 whereas the probe laser intensity is increased from I_0 to 10 I_0. The propagation of the vibrational wave-packets over all allowed internuclear distances is monitored with a probe laser of variable intensity to detect the influence of high laser intensities on the molecular potential sensitive to the internuclear distance. In Fig. 9-7a and 9-7b the power spectrum densities of Fast Fourier Transformations at electron energies corresponding to the outer turning point of the wave-packets are shown. For a probe intensity of I_0 only the frequency components of the 2 $^1\Pi_g$ state are seen as expected in the weak-field regime according to the excitation scheme in Fig. 9-1. However, with increasing probe laser intensity a contribution of the A $^1\Sigma_u^+$ state is seen at the outer turning point as displayed in Fig. 9-7b for a probe laser intensity of 6 I_0. An explanation of this resonant behavior is possible in terms of light-induced potentials [67, 70]. The high probe laser intensity also affects the location for the observation of a ground-state wave-packet. As seen from the excitation scheme in Fig. 9-1 one would expect the frequency contributions of the ground-state wave-packet to be at the inner turning point.

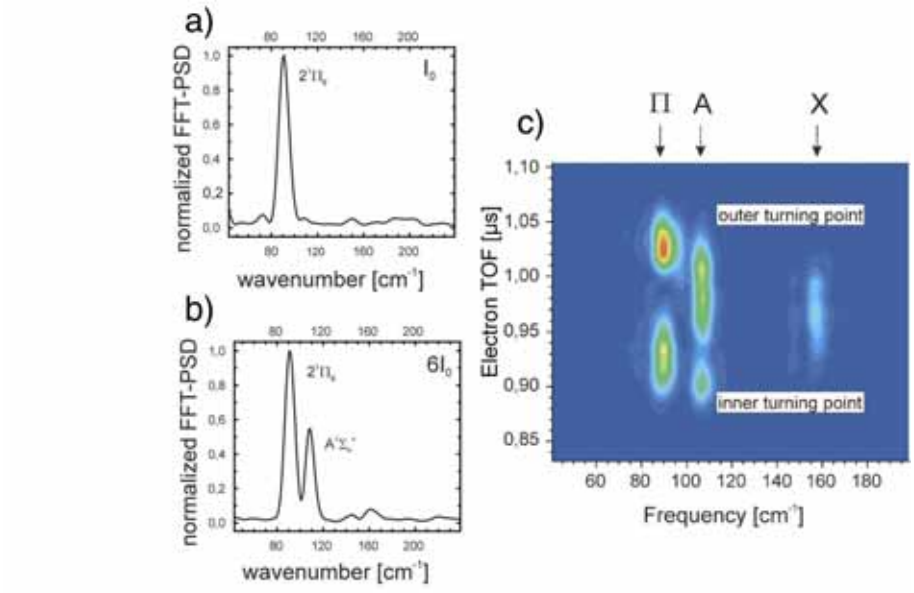

Figure 9-7. Fast Fourier Transformation Power Spectrum Density (FFT-PSD) performed at the outer turning point of the wave-packet motion for the 2 $^1\Pi_g$ state for a pump laser intensity I_0 of approximately 10^{11} W/cm^2. (a) Probe laser intensity is I_0. (b) Probe laser intensity is 6 I_0. Note the additional frequency components due to wave-packet motion in the A $^1\Sigma_u^+$ state. As the FFT is taken on electrons coming from the outer turning point of the 2 $^1\Pi_g$ state, this is a resonance-enhanced contribution and not due to direct non-resonant two-photon ionization out of the A $^1\Sigma_u^+$ state. (c) Spectrogram for same excitation conditions as in (b). In addition to the appearance of the A $^1\Sigma_u^+$ state frequency at the outer turning point, a shift of the ground-state frequency to larger internuclear distances is observed.

Figure 9-7c displays the spectrogram for a pump intensity of 10^{11} W/cm^2 and the 6 times higher probe intensity as depicted in Fig. 9-7b. Obviously, the frequency contributions of the X $^1\Sigma_g^+$ state are shifted to larger internuclear distances. This observation can partly also be interpreted in the frame of light-induced potentials. However, for a full comparison of the experiment with theory the vectorial character of the transition moment for this multi-photon process has to be taken into account as well as additional electronic states in the energetic range of the 2 $^1\Pi_g$ state. Corresponding calculations are currently being performed [71].

Alternatively, the effect of varying the pump laser intensity while keeping the probe laser intensity fixed was also investigated. Figure 9-8a shows the calculated temporal evolution of the population in the X $^1\Sigma_g^+$, A $^1\Sigma_u^+$ and 2 $^1\Pi_g$ states during the pump pulse according to Ref. 63. For low intensities (I_1) the population of the excited states rises monotonicly with time. With increasing intensity (I_2) the onset of Rabi oscillations is observed. Population is transferred efficiently within the electronic states during the

pump pulse. The highest intensity (I_3) was chosen so that the 2 $^1\Pi_g$ state is completely depopulated at the end of the pump pulse thereby performing a "2π" excitation in the terminology of a two state system. Figure 9-8b shows the population of the 2 $^1\Pi_g$ state at the end of the pump pulse as a function of the pump intensity. The experimental realization of such a molecular "2π" excitation is accomplished by increasing the pump laser from I_0 to 2 I_0 and keeping the probe laser intensity at 10 I_0. Figure 9-8c shows sections through the FFT of the photo-electron distribution at the inner turning point for both intensities. At I_0 the contribution at 90 cm^{-1} indicates the presence of population in the 2 $^1\Pi_g$ state. When the pump intensity is doubled, the frequency component at 90 cm^{-1} vanishes thus demonstrating control of the population in the 2 $^1\Pi_g$ state.

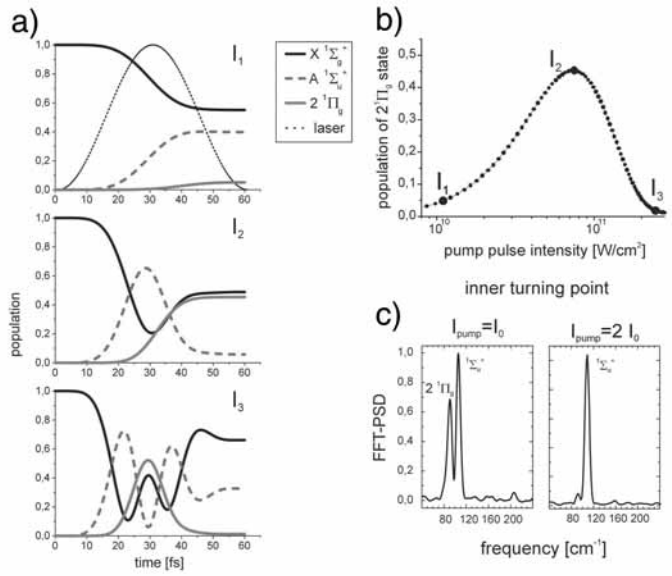

Figure 9-8. a) Temporal evolution of the population in the X $^1\Sigma_g^+$, A $^1\Sigma_u^+$ and 2 $^1\Pi_g$ states during the pump pulse for laser intensities ranging from ~ 10^{10} to 10^{11} W/cm^2. The laser intensity is drawn as a dotted line in the upper figure. b) Population of the 2 $^1\Pi_g$ state at the end of the pump pulse as a function of the laser intensity. c) Experimental verification of the "2π" excitation; pulse width is 70 fs, probe intensity = 10 I_0. Left: $I_{pump} = I_0 = 10^{11}$ W/cm^2. Right: $I_{pump} = 2\ I_0$.

Coherent coupling of electronic states was also investigated in the Na_3 molecule [72]. In the Na_2 prototype further strong-field effects like molecular above threshold ionization [73] and the transition from dissociation along light-induced potentials to field ionization as a function of

laser intensity [74] were investigated in our group with the help of photo-electron spectroscopy and KETOF spectroscopy, respectively.

2.2.2 Coherent coupling of atomic electronic states – control beyond population transfer and spectral interferences

In this section we discuss the control of the quantum mechanical phase in intense laser fields. In order to obtain a clear physical picture, the experiments are performed on an atomic state using a sequence of two intense femtosecond phase-locked laser pulses. The Autler-Townes effect [75, 76] in the photo-ionization of the excited 4*p* state of the K atom is used to follow the temporal evolution of the complex amplitude c_{4p} of the excited state. Coherent control in strong fields beyond (i) population control (as discussed up to now in this chapter), and (ii) spectral interference [20, 77, 78] is demonstrated, since (i) control is achieved without altering the population during the second intense laser pulse, i.e., the population during the second laser pulse is frozen, and (ii) the quantum mechanical phase is controlled without changing the spectrum of the pulse sequence [79]. The control mechanism relies on the interplay of the quantum mechanical phase imparted by the intensity of the first pulse and the optical phase of the second pulse determined by the time delay. Moreover, an uncommon symmetry of the control parameters, *delay* time and *laser intensity*, is observed: with respect to the interferences in the photo-electron spectra the role of time delay and laser intensity is interchangeable for suitable excitation conditions.

In the experiment a sequence of two intense laser pulses is used to excite K atoms in an atomic beam from the 4*s* to the 4*p* state. Simultaneously, the pulses ionize the excited-state atoms to the continuum via two-photon ionization (Fig. 9-9). Photo-electron spectra were taken at various delay times between the two laser pulses and at different laser intensities at a fixed delay time.

The experiments were carried out in a high-vacuum chamber where a beam of atomic potassium K (4*s*) intersects perpendicularly with the femtosecond laser pulses leading to photo-ionization. The released photo-electrons are detected employing a magnetic bottle time-of-flight electron spectrometer. The 785 nm, 30 fs FWHM laser pulses provided by an amplified 1 kHz Ti:sapphire laser system are split into two beams using a Mach-Zehnder interferometer. In the first experiment the time delay τ between the pulses is varied in the range 80 to 100 fs with 0.2 fs resolution at a fixed laser intensity I_0 (0.54×10^{12} W/cm^2). In the second experiment the time delay is kept fixed at 98.6 fs, whereas the energy of both beams is varied from 0.7 I_0 to 3 I_0.

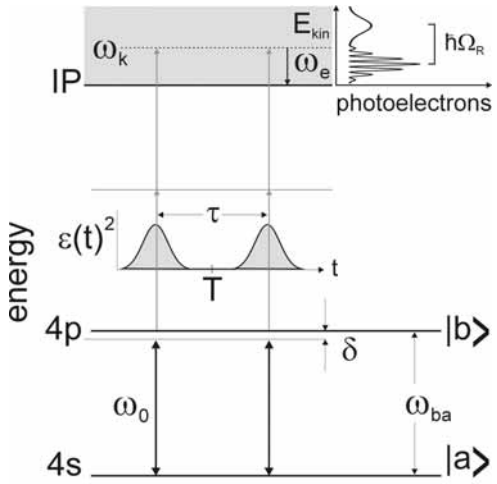

Figure 9-9. Energy level diagram for the excitation of K atoms. A sequence of two intense laser pulses coherently couples the K 4s and 4p states. The photo-electron spectra from simultaneous two-photon ionization provide information on the quantum mechanical phase.

At first, we discuss the results of the experiment using a variable time delay at a fixed laser intensity I_0. Figure 9-10b (left) shows the measured photo-electron spectra as a function of the delay time. Oscillations in the photo-electron signal around the period of the transition frequency are observed. The oscillations of slow and fast photo-electrons are out-of-phase. Sections through the photo-electron distribution were taken along the time delay axis for the fast and the slow photo-electrons [Fig. 9-10a (left)]. In the second experiment the laser intensity was varied but the time delay was fixed [Fig. 9-10b (right)] in order to demonstrate that the control of the interferences is determined by the quantum mechanical phase. The optical spectrum of the pulse sequence remains unchanged for all intensities. A monotonic increase of the splitting of both Autler-Townes components with increasing laser intensity (I_0 to I_2) is observed. The slow electron signal exhibits pronounced oscillations as the intensity is increased.

The observations are discussed in terms of the excited-state amplitudes $c_{4p}(t)$ and the dressed-state picture [60, 80]. The intensity of the first laser is high enough to cause Rabi cycling and, therefore, Autler-Townes splitting of $\hbar\,\Omega_R$ in the photo-electron spectrum. The observed control of interference in the Autler-Townes doublet arises if the intensity of the first pulse is chosen to yield a population of $|c_{4p}(T)|^2 = 0.5$, i.e., a pulse area of $\Theta = (n+0.5)\pi$. The subsequent time evolution ($t > T$) of c_{4p} depends on the optical phase $\omega_0\tau$ of the second laser pulse. If the phase $\omega_0\tau$ takes half integer multiples of π, $|c_{4p}(t)|^2$ is unchanged during the second laser pulse but the quantum mechanical phase is controlled by the second pulse. With regard to photo-

ionization the observations are interpreted in terms of the population of the dressed states. For suitable excitation only one of the dressed states is selectively populated during the second laser pulse and hence interference is only seen in one Autler-Townes component.

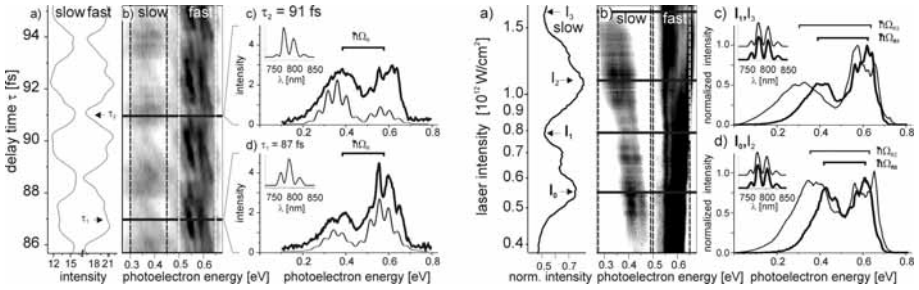

Figure 9-10. Left: (b) Experimental photo-electron spectra as a function of the delay time τ. (a) Sections through the photo-electron distribution along the time delay axis. (c) and (d) Photo- electron spectra at 87 and 91 fs. Right: (b) Measured photo-electron spectra as a function of the laser intensity (normalized) at a fixed delay time. (a) Sections through the photo-electron distribution along the laser intensity axis. (c) and (d) Photo-electron spectra at different laser intensities. The insets show the corresponding optical spectra.

The control mechanism combines phase control and high-intensity effects through the use of phase-locked pulses and intensities that are large enough to cause Rabi cycling. We believe that such mechanisms are at play in many other circumstances as well and that they open the door to a deeper understanding of quantum control in intense laser fields. Especially, the combination of phase modulation of intense laser pulses with well defined model systems will provide insights into the physical mechanisms driving the strong-field control in "open-loop" and "closed-loop" experiments.

3. MANY-PARAMETER CONTROL IN THE GAS PHASE

After the above discussion of one-parameter control schemes on prototypal small systems, we now turn to more complex molecules. Since a large number of degrees of freedom needs to be considered, the external control fields necessarily also have to exhibit more complexity. In general, it will not be sufficient to vary a single control parameter such as a pump-probe delay time. Instead, multi-parameter spectral phase shaping of femtosecond laser pulses is employed, using an automated learning loop and experimental feedback.

3.1 Closed-Loop Femtosecond Pulse Shaping

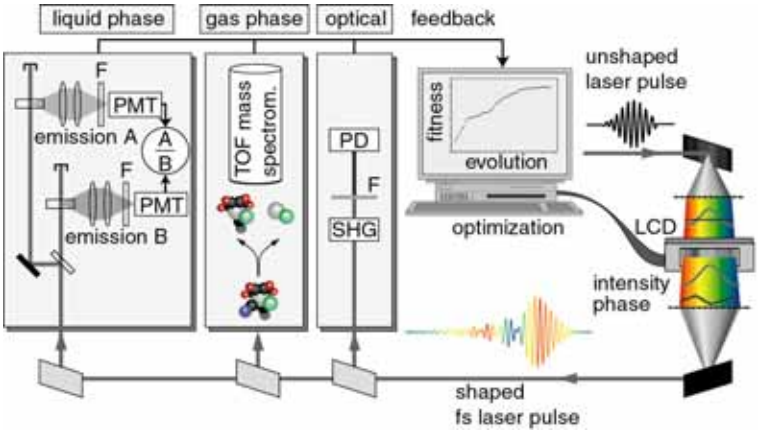

Figure 9-11. Experimental set-up. A femtosecond pulse shaper (right side) is used to generate phase-modulated laser pulses for closed-loop adaptive quantum control. Depending on the type of experiment, experimental feedback signals may be collected from purely optical signal processing (second-harmonic generation, SHG, detected in a photodiode, PD), from gas-phase time-of-flight (TOF) mass spectrometry, or from liquid-phase emission spectroscopy (where the signals are detected after filtering with photomultiplier tubes, PMT). These signals are processed in a computer learning algorithm (based on an evolution strategy approach) which iteratively improves the applied laser pulse shape until an optimum is reached.

The experimental set-up of adaptive femtosecond quantum control is shown in Fig. 9-11. A femtosecond laser pulse shaper (right side of the figure) is used to impose specific spectral phase modulations [16, 17, 81]. The device consists of a zero-dispersion compressor in a 4f-geometry, which is used to spatially disperse and recollimate the femtosecond laser pulse spectrum. Insertion of a liquid-crystal display (LCD) in the Fourier plane of the compressor provides a mechanism for convenient manipulation of the individual wavelength components. By applying voltages, the refractive indices at 128 separate pixels across the laser spectrum can be changed, and upon transmission of the laser beam through the LCD, a frequency-dependent phase is acquired. In this way, an immensely large number of different spectrally phase-modulated femtosecond laser pulses can be produced. In all experiments described below, the spectral amplitudes have not been changed, and therefore the integrated pulse energy remains constant for different pulse shapes. On the other hand, by virtue of the Fourier transformation, spectral phase changes result in phase- and amplitude-modulated laser pulse profiles as a function of time.

The laser pulses can then be used in a number of different experimental schemes. We have implemented purely optical experiments as well as control methods in gas-phase and liquid-phase environments. The resulting experimental signals are recorded and processed within a learning algorithm based on the evolution strategy approach [16, 82, 83], which in turn controls and improves the pulse-shaper settings ("closing the loop"). Evolutionary algorithms use concepts from biological evolution to solve complex optimization problems for which simple models do not exist. In short, a particular laser electric field is represented by the array of voltages applied to the LCD in the pulse shaper. This configuration is called the genetic code of one individual. After applying this laser pulse in the experiment and recording the feedback signals, a user-defined "fitness function" delivers a number which describes how well the optimization objective is fulfilled. Individuals out of a randomly initialized population pool are then selected according to their fitness ("survival of the fittest") and allowed to produce offspring by cross-over, mutation, and cloning operators. The new generation of individuals thus inherit good genetic properties and improve their adaptation to the "environment" so that after cycling through the evolutionary loop for many generations, an optimized laser pulse shape results. This method does not require any model for the system's response, and it is capable of working within large optimization parameter sets.

In the case of an optical control experiment, second-harmonic generation (SHG) in a thin nonlinear crystal can be used as the feedback signal. The temporally integrated SHG yield is a measure for pulse intensity and thus (at constant pulse energies) for pulse duration. The shorter the pulse, the more SHG light is detected. Maximization of SHG hence automatically leads to bandwidth-limited (i.e., the shortest possible) laser pulses at a given spectral bandwidth, improving the output from commercial femtosecond laser systems [15-17]. In connection with quantum control experiments, SHG is also used as a "reference signal" measuring pulse duration, as explained in Sect. 3.3.

Control of photodissociation reactions in the gas phase can be carried out by monitoring the photo-fragment yields in a time-of-flight (TOF) mass spectrometer. For this purpose, the shaped laser pulses are focused into a molecular beam of the reactant substance, initiating different fragmentation and ionization processes. Quantitative product analysis at single-mass-unit resolution is possible even for large molecules by employing a reflectron geometry of the spectrometer [84]. Selected mass peaks are then recorded by boxcar averagers, and ratios as well as absolute yields can be optimized within the evolutionary algorithm. The implementation of liquid-phase control is described in Sect. 4.

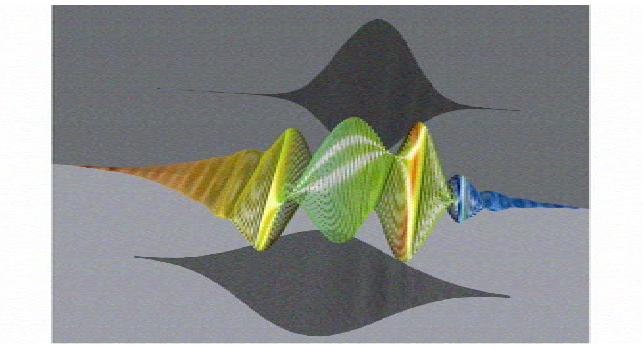

Figure 9-12. Electric field representation for a polarization-shaped femtosecond laser pulse. Time evolves from left to right in this simulation, and electric field amplitudes are indicated by the sizes of the corresponding ellipses. The momentary frequency is indicated by grey shading (or by colours on the front cover), and the shadows represent the amplitude envelopes of component $E(x)$ (bottom) and component $E(y)$ (top) separately.

Further technological development in our group also allows the control of vectorial light polarization on an ultrafast timescale [85-88]. The electric-field polarization (ellipticity and orientation angle), intensity, and oscillation frequency can be varied within a single femtosecond laser pulse with this pulse-shaping device. Without discussing the details of the experimental set-up, it can be said that the basic scheme is similar to the phase-only pulse shaper discussed in this section. However, here a two-layer LCD is used to spectrally manipulate two orthogonal polarization components, and their interference leads to complex polarization profiles in the time domain. An example for such a pulse is shown in Fig. 9-12 (also shown on the front cover of this volume). In this figure, the sizes of the ellipses represent the amplitudes of the electric field at specific times, and the grey shading (or colours on the front cover) indicate the momentary oscillation frequency. It can be seen that the polarization state evolves in a complicated fashion, reaching different transient, linear elliptical and circular polarization regions. Care must be taken in the accurate characterization of these pulse shapers since each optical element between pulse shaper and experiment (such as mirrors or beam splitters) can modify the polarization profile in a non-trivial way [86]. Polarization femtosecond pulse shaping can be considered to be a novel spectroscopic technique, because the temporal as well as three-dimensional spatial properties of quantum-wave functions can potentially be addressed and controlled. Recently, the first adaptive polarization control experiments have been performed on the multiphoton ionization of the potassium dimer prototype [89].

3.2 Control of Product Ratios

One of the initial motivations of molecular quantum control was the desire to be able to "steer" the outcome of chemical reactions such that a certain end-product is produced efficiently while undesired by-products are simultaneously suppressed. This desire can be formulated as the control of photo-product "branching ratios", i.e., the maximization of product yield ratios where the desired substance is placed in the numerator and the undesired molecule in the denominator of the fitness function.

In the first experiments of this kind [12], we have controlled a product branching ratio in the complex organometallic molecule $CpFe(CO)_2Cl$ (where $Cp = C_5H_5$). The two selected separate product channels lead either to the loss of one carbonyl ligand or to almost complete fragmentation, where only the Fe–Cl bond remains. As can be seen in Fig. 9-13, it is then possible to both maximize (5:1) and minimize (1:1) the ratio $CpFeCOCl^+/FeCl^+$ between these two channels compared to unshaped laser pulses (2.5:1). This first example already demonstrates the prospects of this adaptive control technique. Indeed, chemical reaction control (here photodissociation) can be carried out on large molecules. It should be emphasized that control is possible without information about the reaction mechanism or potential energy surfaces. The evolutionary algorithm rather finds the optimal control laser field automatically by means of the experimental feedback signal.

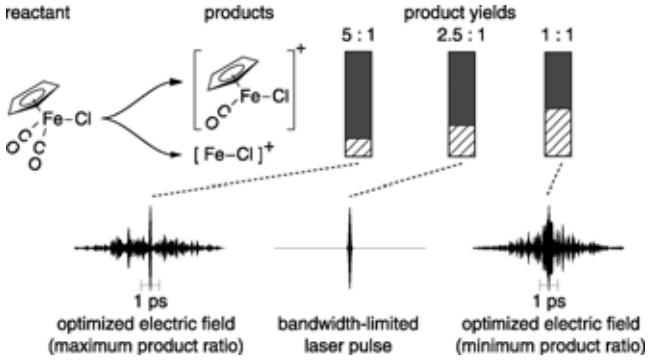

Figure 9-13. Quantum control of the $CpFeCOCl^+/FeCl^+$ product ratio. The top part displays relative yields of the two investigated product channels leading to $CpFeCOCl^+$ (black blocks) and $FeCl^+$ (shaded blocks). The bottom part shows the temporal electric fields leading to a maximum (left) and minimum (right) $CpFeCOCl^+/FeCl^+$ ratio, as well as the electric field of a bandwidth-limited laser pulse (middle) leading to an intermediate branching ratio. The electric fields are calculated by Fourier-transforming the measured laser spectrum and the spectral phase applied by the pulse shaper.

It is also seen that the optimized electric fields after optimization show considerable complexity. A separate analysis [90] revealed that it is not possible to obtain the same or similar results by trivial intensity variation effects; rather the detailed structure is relevant. In further experiments, we have also shown that the optimal electric fields are sensitive with respect to ligand variation [91].

3.3 Bond-Selective Photochemistry

While in the example just shown, the $CpFeCOCl^+/FeCl^+$ photodissociation reaction branching ratio was controlled, the question of explicit selective bond breakage was not addressed. In the next example, however, the goal was to control competing reactions in which the bond cleaved in one channel is preserved in the other channel. This would correspond to "real" bond-selective photochemistry (i.e., to break either one or the other bond). The molecule of choice here was CH_2BrCl, and we attempted to break preferentially the stronger C–Cl bond while keeping the weaker C–Br bond intact [92]. While in some polyhaloalkanes such as CH_2BrI, bond selectivity has been achieved with simple one-parameter wavelength tuning of the excitation laser [93], the situation is different in CH_2BrCl, where strong non-adiabatic coupling among competing dissociation channels [94] leads to a loss of photo-product specificity. The question is therefore if in such a situation adaptive control (using complex many-parameter shaped fields at one given central wavelength) could be used to break selectively one of the carbon–halogen bonds.

During evolutionary optimization, it was indeed possible to increase the CH_2Br^+/CH_2Cl^+ ratio by 100% from 0.083 for bandwidth-limited laser pulses to 0.167 for the optimized pulse shape. In order to analyze the effect of different laser pulse shapes on a certain control objective, and especially to investigate the influence of pulse duration, correlation-type diagrams are useful: for each pulse shape during optimization, we simultaneously record several experimental observables and plot their values against each other (Fig. 9-14). In this way it is possible to see if the respective quantities are correlated (i.e., directly related) or independent. Specifically, we use SHG as a "test" quantity, because it represents a simple way to characterize laser pulse intensity. The presence or absence of correlations of SHG with the optimization objective then tells us whether the control mechanism is intensity dependent in a simple fashion or not.

In the present example of CH_2Br^+/CH_2Cl^+ maximization, the distribution of scatter points evolves along the increasing CH_2Br^+/CH_2Cl^+ axis as a function of generation (Fig. 9-14a). And, even though only a relatively narrow range of SHG yields (i.e., intensities) is explored, significant control

over bond selectivity is achieved (large values along the vertical axis). On the other hand, if SHG is maximized in a comparative but independent optimization (leading to the shortest possible laser pulses with the highest pulse intensities), the scatter distribution evolves mainly along the horizontally increasing SHG axis (Fig. 9-14b). A large number of pulse intensities is sampled (also within the SHG region of Fig. 9-14a), but in this case the CH_2Br^+/CH_2Cl^+ ratio changes only slightly during this variation. This result shows that the quantum control experiment of selective bond breakage cannot be solved with simple intensity variation as in the SHG experiment. Rather the detailed structure of the electric laser field is relevant.

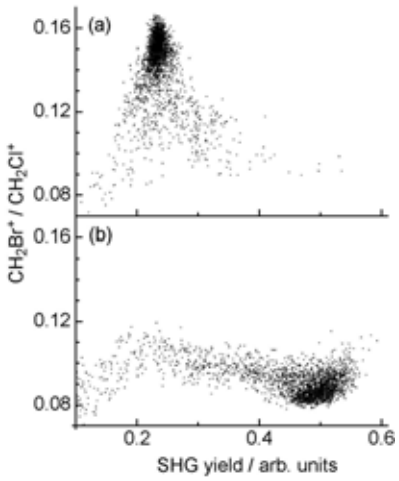

Figure 9-14. Correlation diagrams for selective bond breakage in CH_2BrCl. The value of the CH_2Br^+/CH_2Cl^+ branching ratio is plotted versus second-harmonic generation (SHG) yield for all laser pulses explored in the two optimizations of (a) CH_2Br^+/CH_2Cl^+ maximization and (b) SHG maximization.

Generalized concepts of correlation diagrams can shed further light on the fundamental processes involved in quantum control. For example, one could explore correlations between different molecular fragments, SHG, other nonlinear signals, and also the structure of the electric field itself (using suitable parameterizations).

3.4 Organic Chemical Conversion

Bond-selective photochemistry, as just illustrated, has an important potential use in chemical synthesis for the production of reactive intermediates or the formation of specific products. Due to the generality of

the adaptive approach, this is not limited to any particular class of chemical reactions. With this technique, specific functional groups could be separated from a reactant molecule while leaving the rest of the molecule intact. Such selective reactive steps would be especially helpful in organic chemical synthesis. As an example, we worked with lactic acid ($CH_3CHOHCOOH$). Here, the objective was to efficiently generate ethanol by carboxylic abstraction [95]. This is a prototype example for chemical conversion, where one often desires to remove an acid group, say, without destroying the remainder of the molecule that was just carefully synthesized. We therefore maximized the branching ratio for the removal of COOH versus the removal of CH_3, where the methyl group corresponds to an unwanted side-product arising after cleavage of the "wrong" bond.

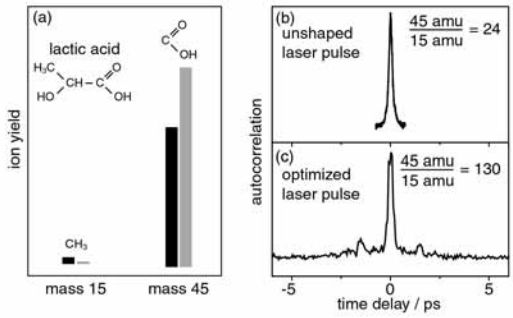

Figure 9-15. Selective bond breaking in lactic acid. The desired product is COOH, the undesired fragment is CH_3. (a) Absolute product yields are shown before (left columns) and after (right columns) optimization. The corresponding branching ratio is increased by a factor of five from the case of (b) unmodulated laser pulses toward (c) optimized laser pulses. The respective pulse shapes are characterized here by intensity autocorrelations.

In Fig. 9-15 it is seen that the $COOH^+/CH_3^+$ ratio can be increased by a factor of five compared to unshaped laser pulses. Thus, bond-selective photodissociation is also achieved in this complex organic molecule. It was possible to break a desired bond without further fragmentation of the remaining molecule. It should also be pointed out that not only the branching ratio (i.e., the purity) has been maximized, but also the absolute yield of the desired fragment was increased compared to the unoptimized situation. In the example shown here, this behavior came "free" with the ratio optimization, but in the general case this need not be true. In other words, optimizing a branching ratio does not necessarily mean that the product yield in the numerator increases while the product yield in the denominator decreases. For practical reasons, however, one often also wants to have explicit control over these absolute yields, i.e., to achieve high efficiency

along with high selectivity. The next section shows how to deal with this situation.

3.5 Multiple Optimization Goals

The philosophy of adaptive control is such that what ever objective we want to achieve with a control experiment one needs to incorporate it into the fitness function. Thus, a higher fitness yield has to represent all of the simultaneous optimization objectives at once. We investigated this in the example of the photofragmentation/photoionization of $Fe(CO)_5$, where we explicitly dealt with the relation between the control of relative product yields (i.e., ratios) versus absolute yields [51]. For this purpose, we defined a generalized fitness function of the form $f(x,y) = ax/\max\{y,y_n\} + bx + cy$, where x and y are the signal heights of wanted and unwanted photo-product, respectively, y_0 is a threshold value which prevents very low signals from below the noise level entering into the fitness calculation (and thus generating physically meaningless high values for the product ratio), and the parameters a, b, c determine the importance of ratio optimization with respect to optimization of the absolute signals.

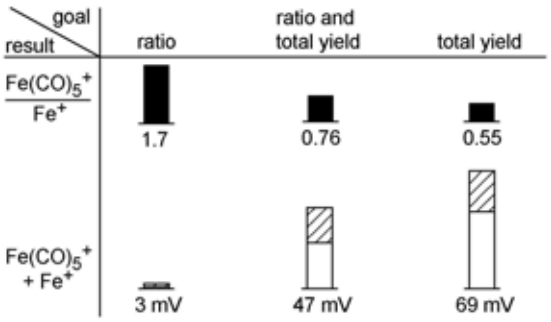

Figure 9-16. Simultaneous control of relative and absolute product yields. This experiment was carried out with 400 nm laser pulses which have been frequency-doubled after the phase shaper. Both the optimized branching ratio (upper row of blocks) and the individual yields (lower row) are shown if the emphasis is put on maximization of the ratio alone (left column), both the ratio and the total yield (middle column), or mainly the total yield (right column). In all cases, the product ratio is higher than that achieved with unmodulated laser pulses.

Our objective here was to maximize the $Fe(CO)_5^+/Fe^+$ yield while simultaneously controlling the individual contributions. Setting $x = Fe(CO)_5^+$ and $y = Fe^+$, the parameters a, b, and c were varied in a systematic fashion, and for each setting an evolutionary optimization was conducted. The results are summarized in Fig. 9-16. If most of the weight is put on the optimization

of $Fe(CO)_5^+/Fe^+$ (left column), the highest value of this ratio within the series is reached. The absolute signal heights, however, are rather small. With increasing weight on those absolute yields (higher values for *b* and *c* with respect to *a*), the total signal increases more and more as desired (albeit at cost to the branching ratio). These results show that it is indeed possible to actively control absolute and relative product yields at the same time. Similarly, if other optimization objectives are desired (e.g., suppression of more than one side-product), the corresponding experimental observables simply have to be included into the fitness function as additional terms. A suitable selection of weighting parameters then determines the relative importance of these goals.In addition to these investigations, we have used $Fe(CO)_5$ to illustrate that, in some simple cases, optimized pulse shapes can be interpreted by comparison with pump-probe mass spectra, yielding insight into the fragmentation dynamics [51].

4. MANY-PARAMETER CONTROL IN THE LIQUID PHASE

Probably the most intriguing initial motivation for quantum control was selective photochemistry in the liquid phase by which macroscopic amounts of chemical substances could be synthesized. While this dream has still not been realized experimentally, a number of breakthroughs toward achieving this goal have been achieved. For example, the possibility of cleaving specifically selected bonds within large molecules has been demonstrated in the gas phase (see Sect. 3). Our first approach to liquid-phase quantum control dealt with selective photo-excitation, monitoring a photo-physical (rather than photo-chemical) observable. We have shown how light pulses can be optimized such that they selectively transfer electronic population within one specific complex dye molecule in solution [96]. This scheme could potentially be used for selective photo-excitation within mixtures of molecules.

Liquid-phase control poses additional difficulties compared to gas-phase experiments. The additional interaction of the reactant molecule with the surrounding solvent is likely to increase the complexity of the quantum dynamical light-induced photo-processes. However, because of the experimental implementation of a closed-loop learning algorithm, optimal laser pulse shapes can always be found under the given experimental conditions, and no detailed information about the dynamics is needed. The experimenter simply has to define a suitable feedback signal which monitors the evolution of the system in that system parameter which is desired to be controlled. For example, with the objective to control excited-state

population, we have used emission spectroscopy to assign the amount of population which was transferred to the emissive state (see Fig. 9-11).

4.1 Control of Metal-Ligand Charge-Transfer Excitation

We have investigated the dye molecule DCM and the organometallic complex $[Ru(dpb)_3](PF_6)_2$, where dpb=4,4'-diphenyl-2,2'-bipyridin, both dissolved in methanol. After excitation with at least two photons at 800 nm and the possibility for additional interaction of the excited species with the electric field of the shaped femtosecond laser pulse, the amount of excited-state population was recorded by monitoring the spontaneous emission signal from each of the two molecules. The objective here was to excite DCM while not exciting (or at least reducing the excitation of) $[Ru(dpb)_3]^{2+}$ [28]. This cannot be done by simple wavelength tuning because the absorption profiles of the two molecules in the relevant energy range show the same wavelength dependence, so that their linear absorption ratio is constant (Fig. 9-17a). Varying the laser intensity is also not a useful control parameter, because the same response is found for both molecules, and the observed emission ratio does not change as a function of pulse energy (Fig. 9-17b). Not even different linear chirps (i.e., laser pulses in which the momentary photon frequency increases or decreases linearly with time) have an effect on the ratio of the excitation probabilities (Fig. 9-17c). Also, the two-photon absorption cross sections have the same wavelength dependence within the laser spectrum, so that scanning the fundamental wavelength does not give selectivity (Fig. 9-17d).

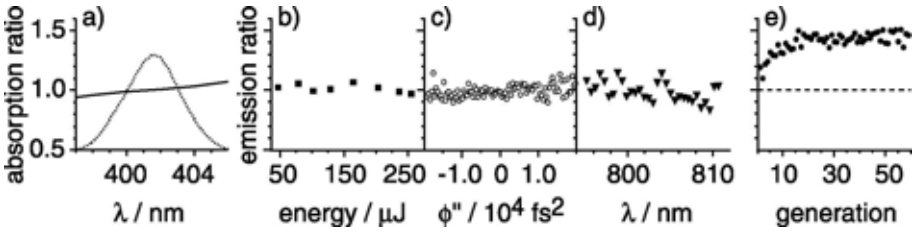

Figure 9-17. Control of liquid-phase molecular excitation. a) The relative DCM/$[Ru(dpb)_3]^{2+}$ linear absorption ratio (solid line) is shown as a function of wavelength. The second-order power spectrum (dotted line) of a bandwidth-limited laser pulse is shown to illustrate possible two-photon transition frequencies. The DCM/$[Ru(dpb)_3]^{2+}$ emission ratio is plotted b) for varying pulse energies of unshaped laser pulses, c) for varying second-order spectral phase (i.e., linear chirp), d) for scanning a symmetric and rectangular window of 5 nm width over the laser spectrum, and e) for many-parameter phase-shaping as a function of generation number within the evolutionary algorithm.

However, selective excitation can be achieved with many-parameter adaptive quantum control in which all 128 LCD pixels are optimized independently. It is shown in Fig. 9-17e how the emission ratio evolves as a function of generation number within the evolutionary algorithm so that finally a 50% increase is observed. Thus it is possible to selectively excite one specific molecular species even within mixtures of molecules with identical absorption profiles. It should be emphasized that control is possible in the presence of complex solute-solvent interactions. The feedback signal rises significantly above the level given by the (unsuccessful) single-parameter schemes (indicated by the dashed line). The failure of the single-parameter schemes indicates that the control mechanism cannot be based on the initial excitation step (which is identical for the two molecules), but exploits the differences in the dynamical wave-packet evolutions on excited-state potential energy surfaces.

4.2 Control of Photo-Isomerization

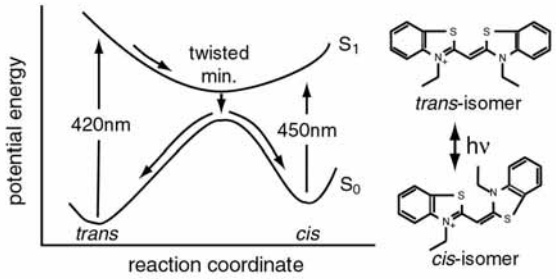

Figure 9-18. Molecular structure of the two isomer configurations and simplified potential energy surface of the cyanine dye NK88.

The next step of the liquid-phase control experiments would be to control a chemical reaction, rather than a photo-physical process. A field of chemistry that has attracted much attention from the coherent control theory community is stereochemistry and in particular the controlled conversion of one enatiomer into the other. A first step towards reaching this goal would be the ability to control geometrical rearrangements of a molecule after the interaction with light. In the context of photo-isomerisation, *cis-trans* isomerisation has attracted much attention because of its importance in chemistry and biology (e.g., primary step of vision) [97]. An intensely

investigated class of molecules that exhibit *cis-trans* isomerization are symmetrical cyanines (see Ref. 98 for a summary). Our molecule 3,3'-diethyl-2,2'-thiacyanine iodide (NK88) also belongs to this class and its thermodynamically stable form is the *trans*-isomer. Irradiated by light around 420 nm the NK88 molecule can undergo the *cis-trans* isomerization process with a certain probability (see Fig. 9-18). Enhancement as well as reduction of the relative yield of *cis*- to *trans*-isomers after photo-excitation can be achieved with optimized femtosecond laser pulses [99]. In order to monitor the amount of achieved control we measured the ratio of generated *cis*-isomers to excited *trans*-isomers by transient absorption spectroscopy in the visible.

5. COHERENT CONTROL OF ELECTRON MOTION

5.1 Coherence Transfer to Free Electrons

After the pioneering electron diffraction experiments of Davisson and Germer [100] which demonstrated the wave properties of matter, interferences of matter waves have been among the most successful confirmation of the wave-particle duality [101]. The interferences of free electron wave-packets generated by a pair of identical, time-delayed, femtosecond laser pulses which ionize excited atomic potassium is reviewed in this section. The experimental results show that the temporal coherence of light pulses is transferred to free electron wave-packets.

The idea of the experiment is shown in Fig. 9-19. A pair of two time-delayed (τ) femtosecond laser pulses generates free electron wave-packets in the ionic continuum (Fig. 9-19a). The time evolution of the electron wave-packet is depicted in Fig. 9-19c for two 30 fs FWHM, 790 nm Gaussian laser pulses with a delay τ of 120 fs. At the end of the laser interaction (350 fs) the outward moving electron wave-packet exhibits a double-peaked structure similar to the exciting laser pulse pair but slightly distorted due to the dispersion of matter waves. Progressing dispersion spreads the partial wave-packets leading to transient interference structures (900 fs). The shape of the wave-packet eventually converges to the photo-electron spectrum taken on a spatial scale (5000 fs). Accordingly, the different arrival times at the detector translate into the spectrum measured in a time-of-flight photo-electron spectrometer.

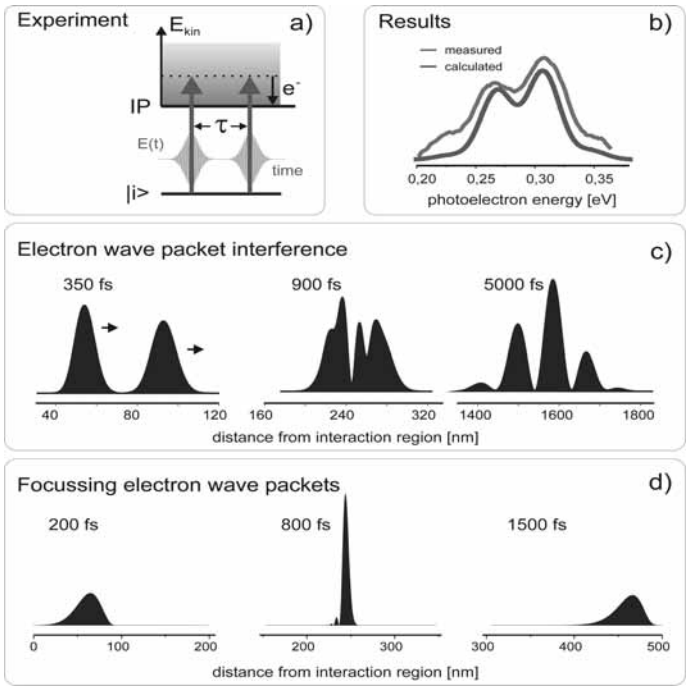

Figure 9-19. Principle of the experiment. (a) A sequence of two time delayed (τ) femtosecond laser pulses creates a double-peaked electron wave-packet. (b) Comparison of experimental and calculated photo-electron spectra with a delay of $\tau = 96$ fs. (c) Time evolution of the double-peaked wave-packet. (d) Spatial focussing of an electron wave-packet: time evolution of a single chirped electron wave-packet.

In Fig. 9-19d calculations of the time evolution of the electron wave-packet created by a single chirped laser pulse (25 fs, -1000 fs^2) demonstrate that electron wave-packets can be spatially focussed. The physical mechanism is based on the generation of chirped electrons, i.e., electrons with low frequency components (slow) first and high frequency components (fast) later. Since the fast components eventually overtake the slow ones (at 800 fs), spatial focussing (at 250 nm) can be achieved. Using stronger chirps, the point of minimal spatial uncertainty can be shifted to much longer distances.

To quantitatively interpret the results a theoretical description of the experiment was given in Ref. 102. The laser electric field $E(t)$ couples the initially prepared 5p state ($|i\rangle$) to the the continuum. In the weak-field regime the spectrum of photo-electrons $P_e(\omega)$ with a kinetic energy of $\hbar\omega_e$ generated by the pulse pair is described by

$$P_e(\omega_e) \propto \left(1 + \cos(\omega_{ph}\tau)\right) PSD(\omega),$$

where $PSD(\omega)$ describes the power spectral density of the driving electric field. From this equation we expect the photo-electron signal at a given photo-electron energy to oscillate sinusoidally as a function of the pulse delay time τ with the respective photon frequency ω_{nh}. Likewise, at fixed delay time τ, fringes in the photo-electron spectrum with an energy separation of h/τ should be visible (see Fig. 9-19b).

The spatio-temporal evolution of the electron wave-packet is described by quasi-free electron wave functions which are approximated by plane waves with a frequency of ω_e

$$\psi(x,t) = \int_0^\infty c(\omega_e, t) e^{i(k_e x - \omega_e t)} d\omega_e$$

and the corresponding wave number $k_e = \sqrt{2m\omega_e}/\hbar$.

The experiments were carried out in a high-vacuum chamber where a beam of atomic potassium K (4s) intersects perpendicularly with the femtosecond laser pulses leading to photo-ionization. The released photo-electrons are detected employing a magnetic-bottle-type electron spectrometer with an energy resolution of 25 meV for electrons with a kinetic energy of 1 eV. The laser beam at the fundamental wavelength – provided by an amplified 1 kHz Ti:Sapphire laser system – is split into two beams. One beam (810 nm) is frequency-doubled to provide 0.2 μJ of 100 fs, 405 nm photons perpendicularly polarized with respect to the TOF-axis. This beam is used to prepare the K (5p) state as the initial state in our experiment. The other beam is delayed by 3 ns (T) and then coupled into a Mach-Zehnder type interferometer to generate a pair of two identical laser pulses (1 μJ, < 10^{12} W/cm^2, 30 fs at 790 nm) with a well-defined temporal spacing τ. The laser intensity was kept low in order to avoid 790 nm multi-photon ionization from the K (4s) ground state. The pair of 790 nm laser pulses has parallel polarization and the electrons are formed in a one-photon ionization process from the K (5p) state. The energy spectrum of the released photo-electrons is recorded as a function of the delay time τ between the two 790 nm laser pulses.

To quantify the experimental results, the fringes in the photo-electron spectrum are directly compared to simulated spectra as demonstrated in Fig. 9-18b. In this comparison, the resolution of the spectrometer (25 meV) was taken into account.

This experiment demonstrates the coherence transfer from light pulses to free electron wave-packets, thus opening the door to a whole variety of exciting new experiments. Our experiments prove that the coherence is preserved on a time scale much longer than the laser interaction. Shaped femtosecond laser pulses have been reported to create optimal wave-packets in order to achieve evolution towards a pre-selected target [12, 22, 61, 103].

Our results show that shaped free electron wave-packets with a predetermined evolution – such as focussed electron wave-packets – can be generated [104]. This may significantly stimulate, for example, experiments on time-resolved electron diffraction [105, 106] and the striking experiments on electron recollision [107]. If the free electron wave-packet is generated by a bandwidth-limited laser pulse and a time delayed shaped laser pulse, one can characterize the shaped laser pulse from the resulting interference pattern in the electron spectrum in analogy to spectral interferometry. This approach has the advantage that it also works in the XUV spectral region and beyond, where pulse characterization methods of complex formed laser pulses are in demand.

5.2 Selective Optimization of High-Order Harmonic Generation

When a highly-intense short laser pulse interacts with a dielectric medium, it is partially converted into the extended ultraviolet (XUV) frequency range, a process termed high-harmonic generation (HHG). It owes its name to the fact that the XUV light generated is emitted coherently into a spectrum consisting of (odd) integer multiples of the fundamental laser frequency.

The origin of this spectral shape lies in the temporal electronic response of the atomic or molecular medium. Every half-cycle of the oscillating laser field, when the field strength is close to the maximum, an electron is tunnel-ionized and driven away from its parent ion. As the sign of the electric field of the laser reverses, the electron starts to accelerate again towards the ion, to which it can possibly return and with which it can recombine [108]. A high-energy photon is then released to carry the excess energy, consisting of the kinetic energy of the returned electron and the ionization potential. The periodic repetition of this ultrashort process (attosecond time scale) leads to the characteristic harmonic line spectrum.

Under standard experimental conditions the XUV harmonic spectrum exhibits another property: starting at lowest orders and moving to higher orders, the high-harmonic intensity drops for a few harmonic orders, then stays roughly constant in the so called plateau region (up to orders ~ 300 [109]) and finally vanishes abruptly at a particular photon energy (cut-off). This large bandwidth of coherent radiation can be used to generate XUV light pulses of a few hundreds of attoseconds duration. These in turn provide a tool to study the electronic dynamics of all kinds of atomic [110] and molecular systems.

To the same extent as this large bandwidth might be beneficial to attosecond pulse generation and observation of electronic dynamics, it is

unfavorable for monitoring and controlling molecular dynamics. For this purpose, a small-bandwidth XUV source would clearly be advantageous. In particular for applications in ultrafast photo-electron spectroscopy a high degree of monochromaticity of the XUV light is a very desirable property. Beyond spectroscopy, also zone-plate nanoscale microscopy using high-harmonic radiation could be improved by exploiting the same property [111].

Thus, it seems reasonable to investigate whether it is possible to control the process of HHG in such a manner that just *one* particular harmonic order is generated while all the others are suppressed. Even beyond this, there is the question of whether it is feasible to *control the overall shape* of the harmonic spectrum. This could open the door to a new era of quantum control, since we could directly steer electrons on their natural time scale [112].

We have been able to show that it is indeed possible not only to enhance specific harmonic orders while suppressing neighboring ones but also to engineer the harmonic XUV spectral shape in more general ways [24]. Selective generation and suppression of single and groups of harmonics is feasible. Our work can be regarded as the first significant step towards quantum control in the XUV spectral region.

Additionally, our experiments represent a direct example for coherent control of electronic motion, since we are able to control the harmonic spectrum emitted by the extended and nonlinear motion of the electron in the vicinity of its parent ion.

In our set-up [113], we use a deformable membrane mirror to shape our laser pulses. This mirror replaces the commonly used retro-reflecting mirror in the prism compressor installed after a hollow-fiber compression stage. By applying control voltages to each of its nineteen electrodes, we are able to create different surface shapes that translate into different spectral phase functions of the laser pulse. A hollow-fiber set-up [114] is used for HHG. Aluminum filters are employed to separate the harmonic light from the intense fundamental laser pulse. For spectral analysis, we use a grazing incidence spectrometer equipped with a backside-illuminated charge-coupled-device camera. A computer is used to read out the spectrometer and to control the deformable mirror. An evolutionary algorithm (Sect. 3.1) [16] iteratively optimizes the harmonic spectrum towards a given shape criterion. This is done by maximizing the fitness function which is a map of the spectrum onto a scalar number. It increases when the spectrum comes closer to the desired shape.

Results of a typical shape optimization experiment are presented in Figs. 9-19a-c. Our goal was to selectively enhance the 25th harmonic order (integrated spectral signal in region A indicated in Fig. 9-20) while at the

same time suppressing the generation of neighbouring orders (region B). The intensity of the 25th harmonic increased by a factor of four while neighboring orders are a factor of three less intense. It is thus possible to generate single harmonic orders with high brightness. We show the fitness of the fittest individual along with the average fitness for each population. To monitor the stability, we plot the fitness of the pulse shape obtained with our reference mirror shape in Fig. 9-20c. The reference mirror shape is obtained when all actuators are set to the same voltage level. We need to define this as a reference since only then the mirror does allow for introduction of both positive and negative surface curvature. The set-up was manually optimized for maximum harmonic output (spectrum shown in Fig. 9-20a) for the reference mirror shape prior to running the optimization algorithm.

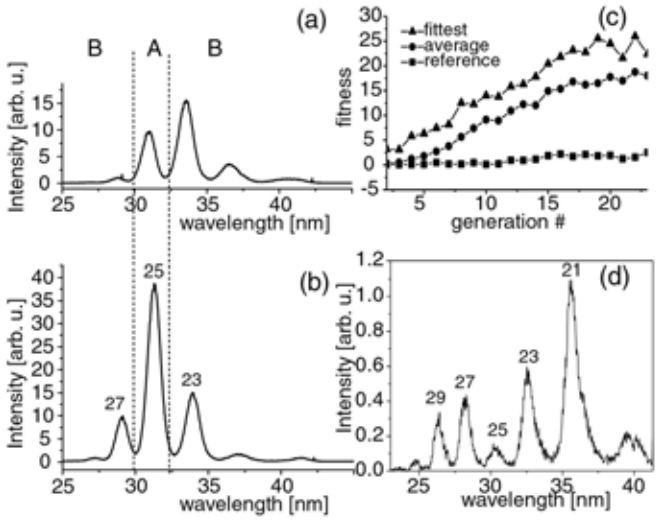

Figure 9-20. Engineering of coherent XUV spectra by controlling electron motion. Optimization experiments were carried out to maximize (a-c) and to minimize (d) single selected harmonics. The fitness of the fittest laser pulse shape increases during the run of the evolutionary algorithm. The reference pulse shape stays at a constant value, indicating stable experimental conditions.

However, a much larger degree of control is possible. Not only can we enhance a particular harmonic, but we already demonstrated isolated harmonic emission at different orders as well as selective generation of groups of harmonics. Another example is the selective minimization of a harmonic, which is depicted in Fig. 9-20d.

We performed simulations based on the solution of the Schrödinger equation for a one-dimensional model atom to elucidate structural changes

of the produced XUV pulses in the time domain. The same evolutionary optimization strategy as employed in the experiments was used for the simulation both for enhancement (Fig. 9-21a) and suppression (Fig. 9-21b) of a single harmonic order (in this case the 23rd). The corresponding trains of attosecond pulses are shown in Fig. 9-21 beside the optimized spectra. Although the changes in the infrared driver pulses are miniscule, the temporal XUV structure changes dramatically, demonstrating comprehensive control over XUV-pulse shape. Remarkably, the ratio of suppressed harmonic orders versus enhanced ones is much less than in the experiments. This agrees with common theoretical knowledge about the single-atom response and proves that controlling spatial propagation effects is important to generate arbitrarily shaped XUV-spectra and attosecond pulses.

We are confident that these findings about control over coherent XUV spectra represent a key to open up a new field of quantum control. The controllable frequency ranges and bandwidths match typical values associated with electronic inner shell processes and electron dynamics in general. Not only can basic molecular vibration and rotation be addressed using femtosecond infrared laser pulses but we can now directly engineer electronic states for further applications.

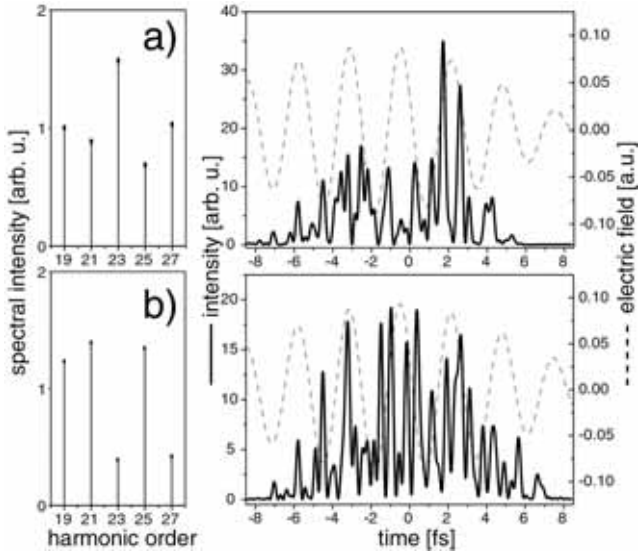

Figure 9-21. Simulation results of coherent XUV engineering. Selective optimization of the 23rd harmonic order with respect to its neighbouring orders. Both relative maximization (a) and minimization (b) were achieved. The corresponding XUV pulse shapes are plotted to the right. The temporal structure of the XUV pulses changes dramatically even though the infrared driving laser pulses are only slightly modified.

6. CONCLUSIONS

In this chapter, we have described femtosecond coherent control techniques and their experimental applications to a variety of quantum systems. Several research routes are pursued in this field. One of the objectives is to provide a basic understanding of mechanisms and control scenarios by investigating suitable model systems. The variation of a limited and small number of control parameters such as pulse intensities, pump-probe delay times, or linear chirp provides new insight into the nature of light-induced dynamics. In most cases, the analysis can be carried out in a wave-packet picture because the spectrally broad femtosecond pulses excite a coherent superposition of energy eigenstates. For multi-photon excitation, higher-order spectral interferences also have to be taken into account. For strong-field interactions, additional effects such as light-induced potentials or the control of quantum phase beyond population transfer and spectral interferences have to be considered. The control "elements" discussed separately in these small-scale model systems can be employed in an optimally combined fashion by using adaptive femtosecond pulse shaping.

The ability to control the spectral-temporal characteristics of light fields in a sophisticated manner has led to a number of experimental breakthroughs. Here the main objective is to reach a specific "target state" of quantum systems. For example, the target can be a certain product distribution after photochemical reactions. Using an automated learning algorithm with experimental feedback, it is indeed possible to control the photodissociation of complex molecules in the gas phase. In the liquid phase additional complications arise due to solute-solvent interactions, but nevertheless selective photo-excitation was achieved, paving the way toward bimolecular reaction control with macroscopic yields.

Apart from their application in atomic or molecular dynamics, femtosecond coherent phase properties can also be transferred onto the motion of free electrons, allowing shaped electron wave-packets to be created. In the case of high-harmonic generation, excitation with adaptively shaped femtosecond pulses leads to tailored XUV spectra, thus making the tools of shaped electric fields also available for the control of inner-shell processes on an attosecond timescale.

Quantum control tells us a lot about the investigated systems and fundamental light-matter interactions. In this sense, it can be considered a sophisticated spectroscopic tool. After the initial suggestions in the late 1980s and many more theoretical investigations, we now witness a huge increase in experimental results. The ability to "make" certain photo-chemical or photo-physical states has been demonstrated in many systems, as more and more groups world-wide join this exciting research field. One

challenge for the future is certainly the realization of reaction control in liquids where specific bonds are broken and others are formed. This could lead to applications in the pharmaceutical industry. But also in "understanding" the underlying processes advances have been made, although there are still many questions to be addressed.

In general, the coherent control of quantum dynamics with tailored femtosecond light fields opens many perspectives in fundamental and applied sciences. Wherever femtosecond light-matter interaction plays a role in physical, chemical, or biological processes, or even in material sciences, specifically shaped laser pulses can be used to increase contrast and efficiency, and to introduce selectivity in a very general sense.

Acknowledgements

This work would not have been possible without the dedicated efforts of many co-workers.

Financial support of the Gerber group came from various sources over the last years, namely from the European Coherent Control Network (COCOMO): HPRN-CT-1999-00129, the German–Israeli Cooperation in Ultrafast Laser Technologies (GILCULT): FKZ-13N7966, the Sonderforschungsbereich 347 (Universität Würzburg): "Selektive Reaktionen metallaktivierter Moleküle", and the "Fonds der chemischen Industrie". The Baumert group acknowledges financial support by the DFG and the NRC-Helmholtz program.

References

1. *Nobel Prize in Chemistry* 1999. Ref. Type: Internet Communication.
2. W. S. Warren, H. Rabitz and M. Dahleh, *Science* **259**, 1581 (1993).
3. R. J. Gordon and S. A. Rice, *Ann. Rev. Phys. Chem.* **48**, 601 (1997).
4. S. A. Rice and M. Zhao, *Optical Control of Molecular Dynamics* (Wiley, New York, 2000), pp. 496-497.
5. H. Rabitz, R. de Vivie-Riedle, M. Motzkus and K. Kompa, *Science* **288**, 824 (2000).
6. M. Shapiro and P. Brumer, in *Advances in Atomic, Molecular, and Optical Physics*, B. Bederson and H. Walther, Eds. (Academic Press, London, 1999), vol. 42.
7. T. Brixner, N. H. Damrauer, G. Gerber, in *Advances in Atomic, Molecular, and Optical Physics*, B. Bederson and H. Walther, Eds. (Academic Press, London, 2001), vol. 46.
8. D. J. Tannor, *Introduction to Quantum Mechanics: A Time-Dependent Perspective* (University Science Press, Sausalito, 2004).
9. M. Shapiro, I. Khavkine, M. Spanner and M. Y. Ivanov, *Phys. Rev. A* **67**, 13406 (2003).
10. T. Brixner and G. Gerber, *Chem. Phys. Chem.* **4**, 418 (2003).
11. C. J. Bardeen et al., *Chem. Phys. Lett.* **280**, 151 (1997).
12. A. Assion et al., *Science* **282**, 919 (1998).
13. T. C. Weinacht, J. L. White and P. H. Bucksbaum, *J. Phys. Chem. A* **103**, 10166 (1999).

14. T. Hornung, R. Meier and M. Motzkus, *Chem. Phys. Lett.* **326**, 445 (2000).
15. D. Yelin, D. Meshulach and Y. Silberberg, *Opt. Lett.* **22**, 1793 (1997).
16. T. Baumert, T. Brixner, V. Seyfried, M. Strehle and G. Gerber, *Appl. Phys. B* **65**, 779 (1997).
17. T. Brixner, M. Strehle and G. Gerber, *Appl. Phys. B* **68**, 281 (1999).
18. D. Meshulach, D. Yelin and Y. Silberberg, *J. Opt. Soc. Am. B* **15**, 1615 (1998).
19. T. Brixner, A. Oehrlein, M. Strehle and G. Gerber, *Appl. Phys. B* **70**, S119 (2000).
20. D. Meshulach and Y. Silberberg, *Nature* **396**, 239 (1998).
21. T. Hornung et al., *Appl. Phys. B* **71**, 277 (2000).
22. T. C. Weinacht, J. Ahn and P. H. Bucksbaum, *Nature* **397**, 233 (1999).
23. R. Bartels et al., *Nature* **406**, 164 (2000).
24. T. Pfeifer, D. Walter, C. Winterfeldt and C. Spielmann, submitted (2004).
25. J. Kunde et al., *Appl. Phys. Lett.* **77**, 924 (2000).
26. D. J. Tannor and A. Bartana, *J. Phys. Chem. A* **103**, 10359 (1999).
27. N. Dudovich, D. Oron and Y. Silberberg, *Nature* **418**, 512 (2002).
28. T. Brixner, N. H. Damrauer, P. Niklaus and G. Gerber, *Nature* **414**, 57 (2001).
29. J. L. Herek, W. Wohlleben, R. J. Cogdell, D. Zeidler and M. Motzkus, *Nature* **417**, 533 (2002).
30. D. Oron, N. Dudovich, D. Yelin and Y. Silberberg, *Phys. Rev. Lett.* **88**, 063004 (2002).
31. R. S. Judson and H. Rabitz, *Phys. Rev. Lett.* **68**, 1500 (1992).
32. R. J. Levis, G. M. Menkir and H. Rabitz, *Science* **292**, 709 (2001).
33. T. C. Weinacht et al., *Chem. Phys. Lett.* **344**, 333 (2001).
34. C. Daniel et al., *Science* **299**, 536 (2003).
35. A. Assion, M. Geisler, J. Helbing, V. Seyfried and T. Baumert, *Phys. Rev. A* **54**, R4605 (1996).
36. T. Baumert, B. Buehler, R. Thalweiser and G. Gerber, *Phys. Rev. Lett.* **64**, 733 (1990).
37. T. Baumert, S. Pedersen and A. H. Zewail, *J. Phys. Chem.* **97**, 12447 (1993).
38. T. Baumert, R. Thalweiser and G. Gerber, *Chem. Phys. Lett.* **209**, 29 (1993).
39. M. Shapiro and P. Brumer, *Principles of the Quantum Control of Molecular Processes* (John Wiley & Sons, Hoboken, New Jersey, Ed. 1, 2003).
40. P. Brumer and M. Shapiro, *Chem. Phys.* **139**, 221 (1989).
41. S. Zamith et al., *Phys. Rev. Lett.* **87**, 033001 (2001).
42. T. Baumert, M. Grosser, R. Thalweiser and G. Gerber, *Phys. Rev. Lett.* **67**, 3753 (1991).
43. T. Baumert et al., *J. Phys. Chem.* **95**, 8103 (1991).
44. V. Engel, *Chem. Phys. Lett.* **178**, 130 (1991).
45. R. S. Mulliken, *J. Chem. Phys.* **55**, 309 (1971).
46. D. J. Tannor, R. Kosloff and S. A. Rice, *J. Chem. Phys.* **85**, 5805 (1986).
47. T. Baumert and G. Gerber, *Israel J.* Chem. **34**, 103 (1994).
48. T. Baumert and G. Gerber, *Advances in Atomic, Molecular, and Optical Physics* **35**, 163 (1995).
49. J. L. Herek, A. Materny and A. H. Zewail, *Chem. Phys. Lett.* **228**, 15 (1994).
50. E. D. Potter, J. L. Herek, S. Pedersen, Q. Liu and A. H. Zewail, *Nature* **355**, 66 (1992).
51. M. Bergt, T. Brixner, B. Kiefer, M. Strehle and G. Gerber, *J. Phys. Chem. A* **103**, 10381 (1999).
52. V. Blanchet and A. Stolow, *J. Chem. Phys.* **108**, 4371 (1998).
53. P. Cong, G. Roberts, J. L. Herek, A. Mohktari and A. H. Zewail, *J. Phys. Chem.* **100**, 7832 (1996).
54. K. Takatsuka, Y. Arasaki, K. Wang and V. McKoy, *Faraday Discuss.* **115**, 1 (2000).
55. Y. Arasaki, K. Takatsuka, K. Wang and V. McKoy, *Chem. Phys. Lett.* **302**, 363 (1999).
56. M. Wollenhaupt et al., *Chem. Phys. Lett.* **376**, 457 (2003).

57. T. Seideman, *Ann. Rev. Phys. Chem.* **53**, 41 (2002).
58. L. Wang, H. Kohguchi and T. Suzuki, *Faraday Discuss.* **113**, 37 (1999).
59. J. A. Davies, R. E. Continetti, D. W. Chandler and C. C. Hayden, *Phys. Rev. Lett.* **84**, 5983 (2000).
60. N. V. Vitanov, T. Halfmann, B. W. Shore and K. Bergmann, *Ann. Rev. Phys. Chem.* **52**, 763 (2001).
61. A. Assion, T. Baumert, J. Helbing, V. Seyfried and G. Gerber, *Chem. Phys. Lett.* **259**, 488 (1996).
62. V. Engel, *Comp. Phys. Comm.* **63**, 228 (1991).
63. Ch. Meier and V. Engel, in *Femtosecond Chemistry*, J. Manz and L. Woeste, Eds. (VCH, Weinheim, 1995), Chap. 11.
64. S. De Silvestri, P. Laporta and O. Svelto, *IEEE J. Quantum Electron.* **QE-20**, 533 (1984).
65. C. J. Bardeen, Q. Wang and C. V. Shank, *Phys. Rev. Lett.* **75**, 3410 (1995).
66. L. Banares, T. Baumert, M. Bergt, B. Kiefer and G. Gerber, *J. Chem. Phys.* **108**, 5799 (1998).
67. T. Frohnmeyer, M. Hofmann, M. Strehle and T. Baumert, *Chem. Phys. Lett.* **312**, 447 (1999).
68. T. Frohnmeyer, M. Strehle and T. Baumert, *Appl. Phys. B* **71**, 259 (2000).
69. R. J. Levis, G. M. Menkir and H. Rabitz, *Science* **292**, 709 (2001).
70. M. Machholm and A. Suzor-Weiner, *J. Chem. Phys.* **105**, 971 (1996).
71. C. Meier, *Toulouse University, Private Communication* (2004).
72. T. Baumert, J. Helbing and G. Gerber, in *Advances in Chemical Physics – Photochemistry: Chemical Reactions and their Control on the Femtosecond Time Scale*, I. Prigogine and S. A. Rice, Eds. (John Wiley & Sons, Inc., New York, 1997).
73. A. Assion, T. Baumert, J. Helbing, V. Seyfried and G. Gerber, *Phys. Rev. A* **55**, 1899 (1997).
74. A. Assion, T. Baumert, U. Weichmann and G. Gerber, *Phys. Rev. Lett.* **86**, 5695 (2001).
75. S. H. Autler and C. H. Townes, *Phys. Rev.* **100**, 703 (1955).
76. U. Lambrecht, M. Nurhuda and F.H.M. Faisal, *Phys. Rev. A* **57**, R3176 (1997).
77. V. V. Lozovoy, I. Pastirk, K. A. Walowicz and M. Dantus, *J. Chem. Phys.* **118**, 3187 (2003).
78. R. Netz, A. Nazarkin and R. Sauerbrey, *Phys. Rev. Lett.* **90**, 063001 (2003).
79. M. Wollenhaupt et al., *Phys. Rev. A* **68**, 015401-1 (2003).
80. B. W. Shore, *The Theory of Coherent Atomic Excitation*, Volume 1 (Wiley, New York, 1990).
81. A. M. Weiner, *Rev. Sci. Instrum.* **71**, 1929 (2000).
82. D. E. Goldberg, *Genetic Algorithms in Search, Optimization, and Machine Learning* (Addison-Wesley, Reading, 1993).
83. H.-P. Schwefel, *Evolution and Optimum Seeking* (Wiley, New York, 1995).
84. B. A. Mamyrin, *Int. J. Mass Spectrom. Ion Processes* **131**, 1 (1993).
85. T. Brixner and G. Gerber, *Opt. Lett.* **26**, 557 (2001).
86. T. Brixner, G. Krampert, P. Niklaus and G. Gerber, *Appl. Phys. B* **74**, S133 (2002).
87. T. Brixner, *Appl. Phys. B* **76**, 531 (2003).
88. T. Brixner, N. H. Damrauer, G. Krampert, P. Niklaus and G. Gerber, *J. Opt. Soc. Am. B* **20**, 878 (2003).
89. T. Brixner et al. *Phys. Rev. Lett.* **92**, 208301 (2004).
90. T. Brixner, B. Kiefer and G. Gerber, *Chem. Phys.* **267**, 241 (2001).
91. M. Bergt, T. Brixner, C. Dietl, B. Kiefer and G. Gerber, *J. Organomet. Chem.* **661**, 199 (2002).
92. N. H. Damrauer et al., *Eur. Phys. J. D* **20**, 71 (2002).

93. L. J. Butler, E. J. Hintsa, S. F. Shane and Y. T. Lee, *J. Chem. Phys.* **86**, 2051 (1987).
94. D. G. Abrashkevich, M. Shapiro and P. Brumer, *J. Chem. Phys.* **116**, 5584 (2002).
95. T. Brixner, N. H. Damrauer, G. Krampert, P. Niklaus and G. Gerber, *J. Mod. Optics* **50**, 539 (2003).
96. T. Brixner, N. H. Damrauer, B. Kiefer and G. Gerber, *J. Chem. Phys.* **118**, 3692 (2003).
97. Q. Wang, R. W. Schoenlein, L. A. Peteanu, R. A. Mathies and C. V. Shank, *Science* **266**, 422 (1994).
98. Y. H. Meyer, M. Pittman and P. Plaza, *J. Photochem. Photobiol. A* **114**, 1 (1998).
99. G. Krampert, G. Vogt, P. Niklaus and G. Gerber, *submitted to Nature* (2004).
100. C. Davisson and L. H. Germer, *Phys. Rev.* **30**, 705 (1927).
101. L. de Broglie, Thesis, Masson & Cie, Paris (1924).
102. M. Wollenhaupt, A. Assion, D. Liese, C. Sarpe-Tudoran and T. Baumert, *Phys. Rev. Lett.* **89**, 173001-1 (2002).
103. C. J. Bardeen et al., *J. Phys. Chem. A* **101**, 3815 (1997).
104. J. C. Delagnes and M. A. Bouchene, *J. Phys. B* **35**, 1819 (2002).
105. J. C. Williamson, M. Dantus, S. B. Kim and A. H. Zewail, *Chem. Phys. Lett.* **196**, 529 (1992).
106. H. Ihee et al., *Science* **291**, 458 (2001).
107. V. R. Bhardwaj, D. M. Rayner, D. M. Villeneuve and P. B. Corkum, *Phys. Rev. Lett.* **87**, 253003-1 (2001).
108. P. B. Corkum, *Phys. Rev. Lett.* **71**, 1994 (1993).
109. C. Spielmann et al., *Science* **278**, 661 (1997).
110. M. Drescher et al., *Nature* **419**, 803 (2002).
111. M. Wieland et al., *Appl. Phys. Lett.* **81**, 2520 (2002).
112. R. Kienberger et al., *Science* **297**, 1144 (2002).
113. T. Pfeifer, U. Weichmann, S. Zipfel and G. Gerber, *J. Mod. Optics* **50**, 705 (2003).
114. A. Rundquist, C. G. Durfee III, Z. Chang, C. Herne and S. Backus, *Science* **280**, 1412 (1998).